ICARUS **122,** 288–315 (1996)
ARTICLE NO. 0126

# The Rate of Iron Sulfide Formation in the Solar Nebula

DANTE S. LAURETTA, DANIEL T. KREMSER, AND BRUCE FEGLEY, JR.

*Department of Earth and Planetary Sciences, Campus Box 1169,Washington University, One Brookings Drive, St. Louis, Missouri 63130-4899*
E-mail: bfegley@planet.win.net

Received May 25, 1995; revised October 6, 1995

**The kinetics and mechanism of the reaction $H_2S(g) + Fe(s) = FeS(s) + H_2(g)$ was studied at temperatures and compositions relevant to the solar nebula. Fe foils were heated at 558–1173 K in $H_2S/H_2$ gas mixtures (~25 to ~10,000 parts per million by volume (ppmv) $H_2S$) at atmospheric pressure. Optical microscopy and X-ray diffraction show that the microstructures and preferred growth orientations of the Fe sulfide scales vary with temperature and $H_2S/H_2$ ratio. Initially, compact, uniformly oriented scales grow on the Fe metal. As sulfidation proceeds, the scales crack and finer grained, randomly oriented crystals grow between the metal and the initial sulfide scale. The composition of the scales varies from $Fe_{0.90}S$ to FeS with temperature and $H_2S/H_2$ ratio, in agreement with thermodynamic calculations. The weight gain and thickness change of the samples give nearly identical measures of the reaction progress. Sulfide layers formed in 25–100 ppmv $H_2S$ grow linearly with time. Iron sulfides formed in ~1000 ppmv $H_2S$ originally grow linearly with time. Upon reaching a critical thickness growth follows parabolic kinetics. Iron sulfide formation in 10,000 ppmv $H_2S$ also follows parabolic kinetics. The linear rate equation for sulfidation of Fe grains (≤20 $\mu$m diameter) in the solar nebula is $d(FeS)/dt = k_f P_{H_2S} - k_r P_{H_2}$ (cm hour$^{-1}$). The forward and reverse rate constants are (cm hour$^{-1}$ atm$^{-1}$) $k_f = 5.6(\pm 1.3)\exp(-27950(\pm 7280)/RT)$ and $k_r = 10.3(\pm 1.0)\exp(-92610(\pm 350)/RT)$, respectively. The activation energies for the forward and reverse reactions are ~28 kJ mole$^{-1}$ and ~93 kJ mole$^{-1}$, respectively. FeS formation in the solar nebula is rapid (e.g., ~200 years at 700 K and $10^{-3}$ bars total pressure for 20 $\mu$m diameter Fe grains) as predicted by simple collision theory models of FeS formation.** © 1996 Academic Press, Inc.

## INTRODUCTION

Chemical reactions between gases and grains in the solar nebula played a major role in establishing the chemistry and mineralogy of the material which later formed the planets, their satellites, and the other bodies in the solar system. Over 30 years of meteorite studies (reviewed in Kerridge and Matthews 1988) and chemical equilibrium modeling of nebular chemistry (e.g., Lord 1965; Larimer 1967; Lewis 1972) demonstrate that evidence of nebular chemical reactions is preserved, with varying degrees of alteration by subsequent processes such as thermal metamorphism and aqueous alteration, in chondritic meteorites.

Despite the many advances made using meteorite studies and theoretical models to shape our understanding of the solar nebula and to constrain conditions (e.g., temperature, pressure, and composition) in it, virtually nothing is known about the rates at which chemical reactions between gases and grains took place in the solar nebula. Such kinetic data are fundamental for addressing first order questions such as how volatiles were retained by the terrestrial planets.

Simple collision theory (SCT) models of gas–grain kinetics in the solar nebula were first presented by Fegley (1988). This SCT modeling considered the rates of gas–grain reactions that were previously predicted by thermodynamic calculations to form three important volatile-bearing phases in chondrites: hydrated silicates, magnetite, and troilite. The SCT models assumed that metal and silicate grains were monodispersed spheres comparable in size to interstellar dust and fine-grained meteorite matrix (~0.1 $\mu$m radius). The kinetic theory of gases and kinetic data from the materials science literature were used to estimate the reactive fraction of collisions and to calculate the chemical lifetime ($t_{chem}$) of the different reactions. Unless the $t_{chem}$ value for a reaction is less than or equal to the nebular lifetime, the reaction is too slow to take place in the solar nebula. Current estimates of the solar nebula lifetime are 0.1–10 million years (Podosek and Cassen 1994). The SCT models predicted that the $t_{chem}$ value for hydrated silicate formation is about 4.5 billion years, that the $t_{chem}$ for magnetite formation is about 320,000 years, and that the $t_{chem}$ for troilite formation is only 320 years (Fegley 1988). Because gas–grain reaction rates decrease with increasing grain size for SCT models, larger $t_{chem}$ values result if larger grain sizes are assumed. The SCT models of gas—grain chemistry were also applied to clathrate hydrate formation and reactions in the Jovian and Saturnian circumplanetary nebulae (e.g., Fegley 1988; Fegley and Prinn 1989; Prinn and Fegley 1989; Fegley 1993).

Although the SCT models provide new insights into the kinetics of gas–grain reactions in the solar nebula,



0019-1035/96 $18.00
Copyright © 1996 by Academic Press, Inc.
All rights of reproduction in any form reserved.

experimental studies of key reactions such as hydrated silicate formation, magnetite formation, and troilite formation are fundamental for understanding the kinetics and mechanisms of gas–grain reactions in the solar nebula and in other protoplanetary nebulae. Because no prior work has been done, we began a study of gas–grain kinetics under temperature, composition (and eventually pressure) conditions relevant to the solar nebula. Preliminary results were reported earlier (e.g., Lauretta and Fegley 1994a, 1994b, 1994c; Lauretta *et al.* 1995a, 1995b).

Here we describe a detailed experimental study of the kinetics and mechanism of troilite (FeS) formation via the reaction $H_2S(g) + Fe(s) = FeS(s) + H_2(g)$ at temperatures and compositions relevant to the solar nebula. This study was undertaken for a number of reasons. Sulfur is the tenth most abundant element in solar material and is the second most abundant volatile element in chondritic rock. Chemical equilibrium calculations predict that in the solar nebula, sulfur first condenses as troilite (e.g., Larimer 1967), the most common sulfide found in meteorites.

We first present revised troilite condensation calculations. Then we describe our experimental study and present the results. The data are then used to model Fe sulfide formation kinetics in the solar nebula and to briefly discuss the origin of troilite and pyrrhotite (Fe-deficient FeS) in meteorites and interplanetary dust particles.

## CONDENSATION CALCULATIONS

We reexamined Fe sulfide condensation for two reasons. The first is the recent claim that monoclinic pyrrhotite ($Fe_{0.875}S$)and iron metal coexist in a solar gas (Wood and Hashimoto 1993). This result is contradicted by the phase diagram for the Fe–S system because the sulfide in equilibrium with Fe metal is troilite (Hansen and Anderko 1958). The second reason is the recent publication of new calorimetric data for the enthalpy of formation of troilite and for the heat capacities of four pyrrhotites ($Fe_{0.98}S$, $Fe_{0.90}S$, $Fe_{0.89}S$, and $Fe_{0.875}S$) and troilite (Cemic and Kleppa 1988; Grønvold *et al.* 1991; Grønvold and Stolen 1992). These data and the sulfur activity measurements by Rau (1976) and by Toulmin and Barton (1964) were used by Grønvold and Stølen (1992) to produce an internally consistent set of thermodynamic properties for troilite and for $Fe_{0.98}S$ to $Fe_{0.875}S$. We used their thermodynamic data for Fe sulfides, JANAF data for $H_2S$ and other sulfur gases (Chase *et al.* 1985), and the solar $S/H_2$ ratio of $3.31 \times 10^{-5}$ (Anders and Grevesse 1989; Dreibus *et al.* 1995) to calculate Fe sulfide condensation temperatures via the reaction

$$H_2S(g) + (1 - \delta)Fe(s) = Fe_{1-\delta}S(s) + H_2(g). \quad (1)$$

The activity of $Fe_{1-\delta}S$ was calculated from the equation

$$a_{Fe_{1-\delta}S} = K_1(P_{H_2S}/P_{H_2})a_{Fe}^{1-\delta}, \quad (2)$$

where $1 - \delta$ is the Fe/S atomic ratio in the Fe sulfide ($\delta \sim 0$ in troilite and $0 < \delta \leq 0.125$ in pyrrhotites), $a_i$ is the activity of species $i$, $K_1$ is the equilibrium constant for

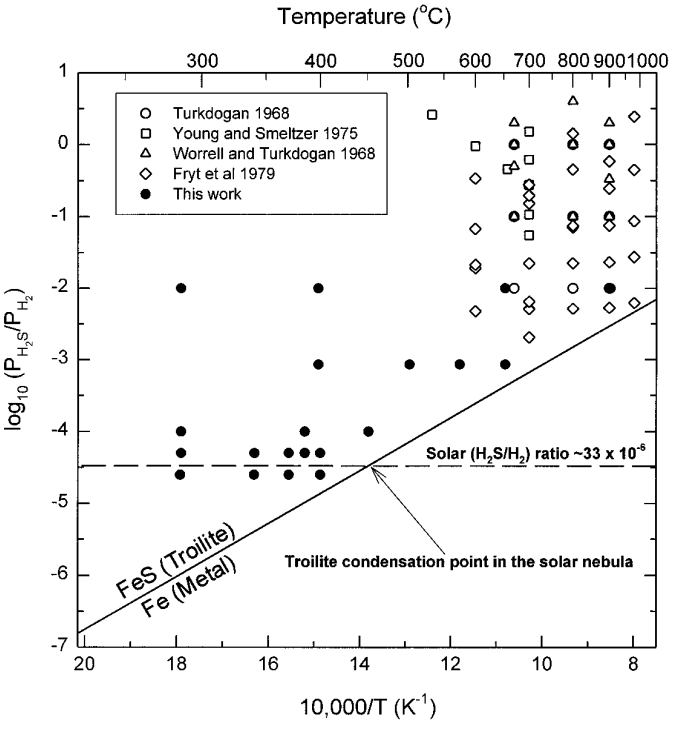


**FIG. 1.** Calculated condensation temperatures for troilite (FeS) as a function of the $H_2S/H_2$ ratio. The horizontal dashed line shows the $H_2S/H_2$ ratio of $\sim 33 \times 10^{-6}$ in solar gas (Anders and Grevesse 1989; Dreibus *et al.* 1995). The two lines intersect at ~713 K where FeS forms from pure Fe metal in a solar gas. FeS forms from solar FeNi alloy at ~710 K. The solid and hollow symbols indicate where our experiments and prior work were done.

**TABLE I**
**Iron Sulfide Condensation Temperatures in the Solar Nebula**[a]

| | Temperature (K)[c] | |
|---|---|---|
| Sulfide | Pure Iron | Solar Fe-Ni Alloy |
| FeS[b] | 713 | 710 |
| $Fe_{0.98}S$[b] | 713 | 710 |
| $Fe_{0.90}S$ | 672 | 670 |
| $Fe_{0.89}S$ | 666 | 664 |
| $Fe_{0.875}S$[d] | 656 | 653 |

[a] Solar $H_2S/H_2 = 3.31 \times 10^{-5}$ (Anders and Grevesse 1989; Dreibus *et al.* 1995).
[b] $Fe_{0.98}S$ condenses less than 1 K below FeS.
[c] The estimated uncertainty is ±10–20°.
[d] Monoclinic $Fe_7S_8$.

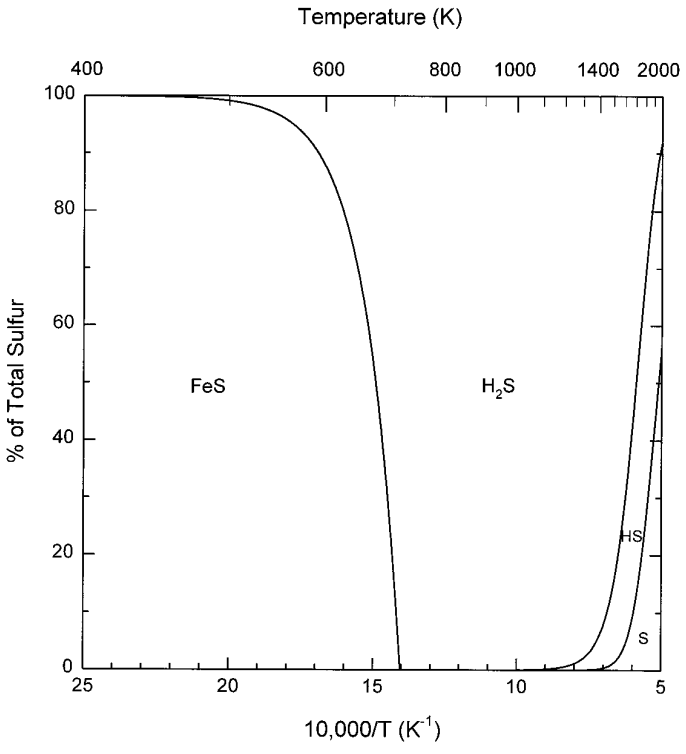


**FIG. 2.** A plot of the calculated distribution of sulfur between gaseous and solid phases from 400 to 2000 K at $10^{-3}$ bars total pressure. Troilite first condenses at the pressure independent temperature of ~713 K in a solar gas. The 50% condensation temperature for sulfur is 674 K, and 100% of the sulfur is incorporated into FeS by 400 K.

reaction (1), and $P_i$ is the partial pressure of gas $i$. The calculations were done both for pure Fe metal and for a solar composition Fe–Ni alloy assuming an ideal solid solution. The resulting condensation temperatures are pressure independent down to $\sim 10^{-11}$ bars, where significant amounts of $S_2$ begin to be produced by $H_2S$ thermal dissociation. For example, the $S_2/H_2S$ molar ratios are ~2% at $10^{-11}$ bars and ~16% at $10^{-12}$ bars at ~720 K for pressures of $10^{-11}$ bars and below.

Table I lists the condensation temperatures for five Fe sulfides ($Fe_{0.875}S$ to stoichiometric FeS) and the Fe/FeS boundary is plotted in Fig. 1. FeS condenses at 713 K, 57 K higher than $Fe_{0.875}S$ and before any other sulfide except $Fe_{0.98}S$, which condenses less than 1 K below FeS. Our FeS condensation temperature is slightly higher than calculated previously because of improvements in the elemental abundances and thermodynamic data (see Table II). The combined uncertainties in the FeS condensation temperature due to uncertainties in the solar $S/H_2$ ratio, in the thermodynamic data for FeS and $H_2S$, in the $a_{Fe}$ value (pure Fe vs solar Fe–Ni alloy), and from the linear fit of $\log_{10} a_{Fe}$ vs $1/T$ are ±10–20 K. Although some of the prior results overlap our FeS condensation temperature within ±10–20°, we recommend use of our value because it is based on updated elemental abundance data (Anders and Grevesse 1989; Dreibus *et al* 1995) and improved thermodynamic data for FeS and pyrrhotites (Gronvold and Stolen 1992).

We also calculated the distribution of sulfur between gas and FeS as a function of temperature (Fig. 2). The 50% condensation temperature for sulfur is 674 K, and 100% of the sulfur is in FeS by 400 K. As discussed later, troilite formation in the solar nebula is rapid. Therefore, the variation in the sulfur content of chondritic material is probably due to separation of grains from the gas (e.g., by accretion into larger bodies) at temperatures above 400 K and not due to slow equilibration of grains with gas (cf. Larimer 1967; Larimer and Anders 1967).

## FE SULFIDE FORMATION EXPERIMENTS

Fe sulfide formation was studied by isothermally heating high purity Fe foils of known weight and surface area in constantly flowing $H_2S$–$H_2$ gas mixtures at ambient atmospheric pressure. About 120 experiments were done to

**TABLE II**
**Comparison of FeS Condensation Temperatures (K) in a Solar Gas**

| Reference | Condensation Temp. (K) | $S/H_2$ (x $10^5$) | Elemental Abundance Data Source | Thermodynamic Data Source |
|---|---|---|---|---|
| This work | 713 | 3.31 | Dreibus et al 1995[c] | Grønvold and Stølen 1992 |
| Sears 1978 | 695 | 3.14 | Cameron 1973 | Robie & Waldbaum 1968 |
| Wai & Wasson 1977 | 685 | 3.14 | Cameron 1973 | Robie & Waldbaum 1968 |
| Grossman 1972 | 700 | 3.89 | Cameron 1968 | Robie & Waldbaum 1968 |
| Larimer 1967 | 680 | 3.72 | Cameron 1963 | Larimer 1967[a] |
| Urey 1952 | ~600 | 2 | Brown 1949 | Urey 1952[b] |

[a] Larimer (1967) calculated the Gibbs free energy of formation of FeS from the elements using data from Richardson and Jeffes (1952) and Rosenqvist (1954).

[b] Urey (1952) calculated the equilibrium constant for the reaction $H_2S + Fe = FeS + H_2$ using data from Rossini *et al.* (1952) and Kelley (1949).

[c] H abundance from Anders and Grevesse (1989).

**TABLE III**
**Iron Sulfidation Experiments**

| Run No. | Temp (K) | Time (hours) | length $a_o$ (cm) | width $b_o$ (cm) | thickness $c_o$ (cm) | wt. gain $\Delta m/m_i$ | Fraction Fe reacted ($\alpha$) gravimetric | geometric | Fe/S ratio in sulfide XRD | Microprobe |
|---|---|---|---|---|---|---|---|---|---|---|
| **Nominal 25 ppm $H_2S$** | | | | | | | | | | |
| 128[a] | 558 | 192 | 1.0654 | 1.0748 | 0.0263 | 2.89E-04 | 0.0089 | n.a. | n.a. | n.a. |
| 126[b] | 558 | 262 | 1.0562 | 1.0764 | 0.0263 | 5.22E-03 | 0.0027 | n.a. | n.a. | n.a. |
| 129[a] | 613 | 192 | 1.0323 | 0.9681 | 0.0264 | 4.37E-04 | 0.0005 | n.a. | n.a. | n.a. |
| 127[b] | 612 | 262 | 1.0072 | 1.0109 | 0.0264 | 1.55E-03 | 0.0007 | n.a. | n.a. | n.a. |
| 130[a] | 643 | 192 | 1.0590 | 0.9111 | 0.0263 | 4.74E-04 | 0.0008 | n.a. | n.a. | n.a. |
| **Nominal 50 ppm $H_2S$** | | | | | | | | | | |
| 48[c] | 558 | 24.2 | 1.1019 | 1.0417 | 0.0292 | 1.02E-03 | 0.0020 | n.a. | 0.965 | n.a. |
| 42[d] | 558 | 96.1 | 0.9996 | 0.9704 | 0.0544 | 4.07E-03 | 0.0070 | n.a. | 0.993 | 0.967 |
| 45[e] | 558 | 222.4 | 0.9791 | 1.0977 | 0.0287 | 1.76E-02 | 0.0310 | n.a. | 0.910 | 0.958 |
| 49[c] | 612 | 24.2 | 0.9921 | 0.9232 | 0.0516 | 1.49E-03 | 0.0030 | n.a. | 0.995 | n.a. |
| 43[d] | 616 | 74.5 | 0.9409 | 1.0354 | 0.0524 | 2.31E-02 | 0.0040 | n.a. | n.a. | 0.957 |
| 46[e] | 614 | 222.4 | 0.9837 | 1.1313 | 0.0282 | 2.94E-02 | 0.0510 | n.a. | 0.920 | 0.941 |
| 122[c] | 643 | 51.5 | 1.0253 | 1.0727 | 0.0263 | 3.63E-04 | 0.0006 | n.a. | n.a. | n.a. |
| 123[c] | 643 | 70.8 | 1.0474 | 0.9678 | 0.0265 | 4.23E-04 | 0.0007 | n.a. | n.a. | n.a. |
| 117[c] | 643 | 96.0 | 0.9807 | 0.9707 | 0.0264 | 1.18E-03 | 0.0020 | n.a. | n.a. | n.a. |
| 124[c] | 658 | 70.8 | 1.0316 | 0.9719 | 0.0262 | 2.73E-04 | 0.0005 | n.a. | n.a. | n.a. |
| 50[c] | 673 | 24.2 | 0.9718 | 1.0224 | 0.0506 | 3.82E-04 | 0.0007 | n.a. | 0.984 | n.a. |
| 152[f] | 673 | 44.1 | 1.0853 | 1.0010 | 0.0557 | 2.28E-04 | 0.0004 | n.a. | 1.002 | 0.975 |
| 125[c] | 673 | 70.8 | 1.0316 | 0.9719 | 0.0262 | 2.73E-04 | 0.0005 | n.a. | n.a. | n.a. |
| 44[d] | 673 | 96.1 | 1.0362 | 1.0425 | 0.0526 | 1.42E-03 | 0.0025 | n.a. | 0.997 | 0.996 |
| 47[e] | 673 | 222.4 | 0.9770 | 1.1134 | 0.0282 | 4.04E-03 | 0.0070 | n.a. | 0.970 | 0.975 |
| **Nominal 100 ppm $H_2S$** | | | | | | | | | | |
| 36[g] | 560 | 27.2 | 0.9631 | 1.0297 | 0.0472 | 1.73E-04 | 0.0003 | n.a. | 0.976 | n.a. |
| 38[h] | 560 | 47.2 | 1.0641 | 1.0248 | 0.0491 | 3.41E-04 | 0.0006 | n.a. | 0.971 | 0.988 |
| 40[h] | 556 | 79.9 | 1.0195 | 0.9916 | 0.0492 | 1.38E-03 | 0.0024 | n.a. | 0.968 | n.a. |
| 37[g] | 656 | 27.2 | 1.0070 | 1.0624 | 0.0469 | 1.18E-03 | 0.0021 | n.a. | 0.999 | n.a. |
| 39[h] | 656 | 47.2 | 1.0287 | 0.8994 | 0.0492 | 1.77E-03 | 0.0031 | n.a. | 1.012 | 0.998 |
| 41[h] | 659 | 79.9 | 1.0196 | 1.0563 | 0.0495 | 3.46E-03 | 0.0060 | n.a. | 0.980 | 0.995 |
| 27[g] | 723 | 10.0 | 1.0218 | 1.0348 | 0.0466 | 2.46E-03 | 0.0043 | n.a. | 1.007 | n.a. |
| 28[g] | 723 | 46.5 | 1.0609 | 1.0072 | 0.0502 | 2.28E-03 | 0.0040 | n.a. | n.a. | 0.952 |
| 29[g] | 723 | 48.6 | 1.0529 | 0.9951 | 0.0465 | 6.51E-03 | 0.0113 | n.a. | 1.007 | n.a. |
| 26[g] | 723 | 96.3 | 1.0349 | 1.0098 | 0.0473 | 6.78E-03 | 0.0118 | n.a. | 0.997 | 0.978 |
| **Nominal 1000 ppm $H_2S$** | | | | | | | | | | |
| 71[i] | 673 | 2.5 | 1.0318 | 1.0362 | 0.0264 | 3.87E-03 | 0.007 | 0.027 | n.a. | 0.998 |
| 55[i] | 673 | 5.0 | 0.9950 | 0.9392 | 0.0268 | 7.53E-03 | 0.013 | 0.045 | n.a. | 0.991 |
| 67[i] | 673 | 12.0 | 1.0758 | 0.9591 | 0.0262 | 1.72E-02 | 0.030 | 0.069 | n.a. | 0.983 |
| 63[i] | 673 | 24.0 | 1.0639 | 1.0092 | 0.0263 | 3.19E-02 | 0.055 | 0.087 | n.a. | 0.982 |
| 59[i] | 673 | 48.0 | 1.1448 | 1.0447 | 0.0266 | 4.83E-02 | 0.084 | 0.128 | n.a. | 0.985 |
| 51[j] | 673 | 447.4 | 1.0220 | 0.9862 | 0.0265 | 3.08E-01 | 0.536 | 0.547 | 0.990 | 0.978 |
| 72[i] | 778 | 2.5 | 1.0181 | 0.9795 | 0.0265 | 1.27E-02 | 0.022 | 0.034 | n.a. | 0.984 |
| 56[i] | 778 | 5.0 | 1.0252 | 0.9741 | 0.0267 | 1.53E-02 | 0.027 | 0.071 | n.a. | 0.987 |
| 23[k] | 778 | 10.0 | 1.0080 | 0.8090 | 0.0248 | 2.70E-02 | 0.047 | 0.105 | 0.998 | 1.006 |
| 68[i] | 778 | 12.0 | 0.9500 | 0.9348 | 0.0261 | 3.56E-02 | 0.062 | 0.111 | n.a. | 0.984 |
| 64[i] | 778 | 24.0 | 1.0257 | 0.9600 | 0.0263 | 5.19E-02 | 0.090 | 0.118 | n.a. | 0.986 |
| 60[i] | 778 | 48.0 | 0.9997 | 1.0096 | 0.0267 | 7.86E-02 | 0.137 | 0.161 | n.a. | 0.987 |
| 24[k] | 779 | 96.5 | 0.9586 | 0.9510 | 0.0250 | 8.47E-02 | 0.147 | 0.123 | 0.992 | 0.989 |
| 52[j] | 778 | 447.4 | 1.0218 | 1.0041 | 0.0263 | 3.20E-01 | 0.557 | 0.605 | 0.999 | 0.982 |
| 16[k] | 850 | 1.0 | 1.0373 | 1.0602 | 0.0241 | 1.46E-02 | 0.025 | 0.143 | n.a. | n.a. |
| 73[i] | 848 | 2.5 | 0.9924 | 1.0055 | 0.0262 | 4.27E-03 | 0.007 | 0.023 | n.a. | 0.961 |
| 57[i] | 848 | 5.0 | 1.0556 | 0.9523 | 0.0268 | 2.06E-02 | 0.036 | 0.075 | n.a. | 0.971 |

**TABLE III**—*Continued*

| Run No. | Temp (K) | Time (hours) | length $a_o$ (cm) | width $b_o$ (cm) | thickness $c_o$ (cm) | wt. gain $\Delta m/m_i$ | Fraction Fe reacted ($\alpha$) gravimetric | geometric | Fe/S ratio in sulfide XRD | Microprobe |
|---|---|---|---|---|---|---|---|---|---|---|
| 69[i] | 848 | 12.0 | 1.0469 | 0.9967 | 0.0265 | 4.94E-02 | 0.086 | 0.091 | n.a. | 0.995 |
| 65[i] | 848 | 24.0 | 1.0321 | 1.0383 | 0.0261 | 8.54E-02 | 0.149 | 0.172 | n.a. | 0.988 |
| 15[k] | 851 | 35.0 | 1.0549 | 1.0461 | 0.0247 | 7.18E-02 | 0.125 | 0.106 | 1.001 | 0.979 |
| 61[i] | 848 | 48.0 | 0.9802 | 0.9718 | 0.0266 | 1.32E-01 | 0.230 | 0.248 | n.a. | 0.981 |
| 17[k] | 848 | 97.1 | 1.0618 | 0.9740 | 0.0246 | 8.88E-02 | 0.155 | 0.324 | 1.000 | 0.977 |
| 53[j] | 848 | 447.4 | 1.0119 | 1.0402 | 0.0264 | 5.61E-01 | 0.977 | 1.000 | 0.995 | n.a. |
| 74[l] | 923 | 2.5 | 1.0469 | 0.9682 | 0.0262 | 1.40E-02 | 0.024 | 0.053 | n.a. | 0.986 |
| 58[i] | 923 | 5.0 | 0.9798 | 0.9709 | 0.0263 | 2.21E-02 | 0.038 | 0.057 | 0.984 | 1.005 |
| 18[k] | 926 | 10.0 | 1.0308 | 0.8810 | 0.0262 | 1.35E-02 | 0.023 | 0.066 | 1.003 | 0.993 |
| 70[i] | 923 | 12.0 | 1.0008 | 0.9853 | 0.0262 | 6.03E-02 | 0.105 | 0.115 | 0.975 | 0.999 |
| 66[i] | 923 | 24.0 | 0.9614 | 1.0010 | 0.0265 | 1.06E-01 | 0.185 | 0.185 | 0.967 | 0.997 |
| 35[k] | 923 | 40.2 | 0.9126 | 0.9993 | 0.0458 | 8.62E-02 | 0.150 | 0.128 | 1.007 | 0.978 |
| 34[k] | 923 | 41.9 | 1.0420 | 1.0105 | 0.0463 | 8.75E-02 | 0.152 | 0.153 | 0.996 | 0.976 |
| 32[k] | 923 | 42.7 | 1.0254 | 0.9571 | 0.0455 | 5.56E-02 | 0.103 | 0.102 | 0.994 | 0.996 |
| 33[k] | 923 | 43.4 | 1.0324 | 1.0493 | 0.0454 | 8.44E-02 | 0.160 | 0.140 | 1.004 | 0.979 |
| 62[i] | 923 | 48.0 | 1.0073 | 1.0255 | 0.0266 | 1.65E-01 | 0.287 | 0.263 | 0.973 | 0.987 |
| 21[k] | 926 | 96.0 | 1.0287 | 0.9110 | 0.0262 | 1.44E-01 | 0.292 | 0.316 | n.a. | 0.981 |
| 54[j] | 923 | 447.4 | 0.9368 | 0.9776 | 0.0262 | 4.64E-01 | 0.808 | 1.000 | 0.995 | n.a. |
| **Nominal 10000 ppm $H_2S$** | | | | | | | | | | |
| 83[l] | 558 | 1.5 | 1.0445 | 1.0048 | 0.0262 | 1.53E-03 | 0.003 | 0.000 | n.a. | n.a. |
| 79[l] | 558 | 6.0 | 1.0081 | 1.0152 | 0.0261 | 6.23E-03 | 0.011 | 0.013 | n.a. | 0.983 |
| 94[l] | 558 | 12.0 | 1.0596 | 0.9849 | 0.0260 | 1.48E-02 | 0.026 | 0.015 | n.a. | 0.981 |
| 75[l] | 558 | 12.0 | 0.9994 | 1.0125 | 0.0259 | 1.52E-02 | 0.026 | 0.036 | n.a. | 1.028 |
| 91[l] | 558 | 18.5 | 1.0491 | 1.0597 | 0.0263 | 1.80E-02 | 0.031 | 0.063 | n.a. | 0.957 |
| 96[m] | 558 | 48.0 | 1.0558 | 0.9973 | 0.0261 | 2.53E-02 | 0.044 | 0.044 | n.a. | 0.984 |
| 99[m] | 558 | 48.0 | 1.0436 | 0.9896 | 0.0262 | 3.42E-02 | 0.060 | 0.038 | n.a. | 0.989 |
| 103[m] | 558 | 72.0 | 1.0002 | 0.9896 | 0.0262 | 4.84E-02 | 0.084 | 0.016 | n.a. | 0.945 |
| 101[m] | 558 | 96.0 | 1.0165 | 0.9934 | 0.0263 | 5.92E-02 | 0.103 | 0.068 | n.a. | 0.916 |
| 107[n] | 558 | 118.3 | 0.9920 | 0.9958 | 0.0262 | 7.64E-02 | 0.133 | 0.081 | 0.926 | 0.924 |
| 109[n] | 558 | 146.1 | 1.0122 | 1.0022 | 0.0261 | 8.95E-02 | 0.156 | 0.073 | n.a. | n.a. |
| 84[l] | 673 | 1.5 | 1.0093 | 1.0273 | 0.0262 | 5.57E-03 | 0.010 | 0.005 | n.a. | 0.972 |
| 80[l] | 673 | 6.0 | 1.0288 | 0.9968 | 0.0260 | 9.04E-03 | 0.016 | n.a. | n.a. | 0.986 |
| 76[l] | 673 | 12.0 | 0.9864 | 0.9965 | 0.0262 | 1.29E-02 | 0.022 | 0.026 | n.a. | 0.948 |
| 95[l] | 673 | 12.0 | 1.0574 | 0.9950 | 0.0260 | 8.27E-03 | 0.014 | 0.006 | n.a. | 1.005 |
| 92[l] | 673 | 18.5 | 1.0581 | 1.0026 | 0.0260 | 1.07E-02 | 0.019 | 0.040 | n.a. | n.a. |
| 97[m] | 673 | 24.0 | 1.0151 | 1.0047 | 0.0263 | 1.74E-02 | 0.030 | 0.014 | n.a. | 0.986 |
| 100[m] | 673 | 48.0 | 1.0078 | 0.9937 | 0.0259 | 3.17E-02 | 0.055 | n.a. | 0.995 | n.a. |
| 104[m] | 673 | 72.0 | 1.0311 | 0.9839 | 0.0263 | 6.66E-02 | 0.116 | 0.076 | n.a. | n.a. |
| 102[m] | 673 | 96.0 | 1.0010 | 0.9517 | 0.0262 | 7.02E-02 | 0.122 | 0.086 | n.a. | n.a. |
| 108[n] | 673 | 118.3 | 1.0121 | 1.0149 | 0.0263 | 1.01E-01 | 0.176 | 0.168 | n.a. | 0.988 |
| 110[n] | 673 | 146.1 | 1.0203 | 1.0051 | 0.0262 | 9.26E-02 | 0.161 | 0.143 | n.a. | 0.981 |
| 85[l] | 923 | 1.5 | 1.0093 | 1.0273 | 0.0262 | 8.63E-02 | 0.150 | 0.144 | n.a. | 0.980 |
| 81[l] | 923 | 6.0 | 1.0311 | 1.0033 | 0.0258 | 2.18E-01 | 0.379 | 0.380 | n.a. | 1.000 |
| 77[l] | 923 | 12.0 | 1.0156 | 0.9906 | 0.0258 | 3.48E-01 | 0.606 | 0.597 | n.a. | 0.994 |
| 93[l] | 923 | 18.5 | 1.0540 | 1.0375 | 0.0263 | 4.70E-01 | 0.819 | 0.787 | n.a. | 0.996 |
| 98[m] | 923 | 24.0 | 1.0216 | 1.0123 | 0.0262 | 5.73E-01 | 0.998 | 1.000 | 0.987 | 0.922 |
| 86[l] | 1,173 | 1.5 | 1.0383 | 0.9959 | 0.0260 | 3.03E-01 | 0.528 | 0.575 | n.a. | 0.983 |
| 82[l] | 1,173 | 6.0 | 0.9999 | 0.9592 | 0.0261 | n.a. | 1.000 | 1.000 | n.a. | n.a. |
| 78[l] | 1,173 | 12.0 | 0.9613 | 0.9975 | 0.0257 | n.a. | 1.000 | 1.000 | 0.991 | n.a. |

[a–n] The $H_2S$ contents (in ppmv) of the different gas cylinders used are as follows: (a) 27/28.4, (b) 29.6/29.8, (c) 53, (d) 51.7, (e) 52.3, (f) 51.4, (g) 100.1, (h) 96.4, (i) 885, (j) 884, (k) 868, (l) 10800, (m) 10900, (n) 9800. n.a. = not analyzed.

**TABLE IV**
**Previous Kinetic Studies of FeS Formation**

| Temperature Range (K) | Gas Composition | Sulfur Fugacity $\log_{10} f_{S2}$ (atm) | | Reference |
|---|---|---|---|---|
| | | min | max | |
| 893-970 | S vapor | - | -1.9 | Hauffe and Rahmel 1952 |
| 923-1173 | S vapor | - | -0.9 | Meussner and Birchenall 1956 |
| 673-823 | $H_2S/H_2$ | -14.8 | -12.3 | Haycock 1959* |
| 983 | S vapor | - | 0 | Bruckman and Romanski 1965 |
| 943-1173 | $H_2S/H_2$ | -6.9 | -3 | Turkdogan 1968 |
| 943-1173 | $H_2S/H_2$/Ar | -6.9 | -2.4 | Worrell and Turkdogan 1968 |
| 773 | S vapor | -3.9 | -0.9 | Strafford and Manifold 1969 |
| 1030-1173 | $COS/CO/CO_2$ | -22.9 | -21.2 | Haugen and Sterten 1971 |
| 973-1173 | S vapor | -1.0 | 0 | Narita and Nishida 1973 |
| 1023-1175 | $COS/CO/CO_2$ | -20.5 | -19.4 | Sterten and Haugen 1973 |
| 806-973 | $H_2S/H_2$ | -6.9 | -5.7 | Young and Smeltzer 1976 |
| 873-1253 | $H_2S/H_2$ | -9.1 | -1.0 | Fryt, Smeltzer and Kirkaldy 1979 |
| 558-1173 | $H_2S/H_2$ | -20.2 | -6.9 | This work |
| 713 | $H_2S/H_2$ | - | -17.0 | Solar gas |

* Experiments done at 40.8 atm total pressure.

determine the effects of temperature and $H_2S/H_2$ ratios on the composition and microstructure of the Fe sulfide formed and on the rate of reaction. The temperatures and $H_2S/H_2$ ratios of the experimental runs are shown as black dots in Fig. 1 and are listed in Table III. As summarized in Table IV, much of the prior work on FeS formation has been done in sulfur vapor or gas mixtures irrelevant to the solar nebula. Furthermore, the prior studies using $H_2S/H_2$ mixtures had $H_2S/H_2$ ratios higher than the solar S/H ratio (e.g., see the hollow symbols in Fig. 1). Iron foils (Johnson–Matthey Puratronic grade 99.998% pure on a metals basis) were carefully weighed (to $\pm 1$ $\mu$g) and measured (to $\pm 0.00025$ cm) and then reacted in vertical (runs 1–34, 37, 39, 41) and horizontal tube furnaces (runs 35, 36, 38, 40, 42–122). In both types of furnaces the samples were suspended next to $Pt/Pt_{90}Rh_{10}$ thermocouples. Over 30 days the temperatures fluctuated by $\leq 1$°C. The total uncertainty in the run temperatures is $\pm$ 3–5° C.

At the start of the experiment the sample was placed into the end of the muffle tube while the tube was flushed with prepurified $N_2$ (>99.998%). After 10 min of flushing with $N_2$, the sample was moved into the hot zone and the furnace was then flooded with prepurified $H_2$ (>99.99%). The sample was annealed in $H_2$ for 24 hr at 750 K. After annealing, the sample was cooled to the run temperature under $H_2$ gas and the furnace was flooded with the $H_2S$–$H_2$ mixture, starting the sulfidation experiment.

The $H_2S$–$H_2$ gas mixtures used were Matheson certified standards (accurate to $\pm 2\%$ of the analyzed value) with nominal $H_2S$ concentrations of 25, 50, 100, 1,000, and 10,000 ppmv. The actual $H_2S$ concentrations are listed in Table III. The gas flow rates were controlled using high accuracy rotameters. The linear flow velocities of ~95 cm/min are rapid enough to avoid gas unmixing by thermal diffusion (Darken and Gurry 1945). Good agreement between predicted and observed Fe/S ratios in the Fe sulfide layers shows that thermal diffusion was not a problem.

At the end of the reaction, the furnace was flooded with $N_2$ gas, and the sample was moved to the cool end of the muffle tube. The sample temperature dropped to 50°C within 5 min. We did not quench the samples more rapidly because the fragile FeS layers might have been damaged and/or lost. Other workers studying oxide layer formation on Fe metal quenched their samples in the same manner (Turkdogan *et al.* 1965).

## CHARACTERIZATION OF REACTED SAMPLES

(*a*) *X-ray diffraction.* XRD patterns were obtained using a Rigaku vertical powder diffractometer with Cu$K\alpha$ ($\lambda$ = 1.540598 Å) radiation and Materials Data Incorporated (MDI) software. In many cases XRD patterns of the layers were taken to identify the sulfide formed (e.g., troilite vs pyrrhotite) and the crystal growth planes. If a thick enough sulfide layer had formed, it was powdered under acetone in an agate mortar and used for precise

measurements of the Fe/S atomic ratio by determining the position of the $d(102)$ peak of the NiAs-type cell (the (114) reflection in the troilite cell or the (866) line in the 5C pyrrhotite superstructure cell). During these measurements silicon powder (NIST 640b) was used as an internal standard. Each sample was measured twice and all data for samples along an isotherm were averaged together. The $1\sigma$ uncertainties on the Fe/S ratios were calculated using small number statistics (Wilson 1952).

(*b*) *Electron microprobe analyses.* Electron microprobe analyses were done with the Washington University JEOL-733 electron microprobe equipped with Advanced Microbeam automation. An accelerating voltage of 15 kV was used with 30 nA beam current and a beam diameter of 1 $\mu$m. X-ray matrix corrections were based on a modified Armstrong (1988) CITZAF routine.

Pyrite ($FeS_2$) was used as a primary standard because it is homogenous and stoichiometric, whereas troilite displays deviations from the ideal stoichiometry (Condit *et al.* 1974; Horwood *et al.* 1976; Rau 1976). Numerous analyses of the $FeS_2$ standard as an unknown yielded Fe/S = 0.500 ± 0.003 ($1\sigma$) while analyses of the FeS standard (Staunton octahedrite troilite) gave Fe/S = 0.982 ± 0.007. Furthermore, the detected X-ray maxima (spectrometer peak position) for Fe and S on the standards and experimental charges were repeatedly compared and found to be identical.

## MICROSTRUCTURE AND MORPHOLOGY OF SULFIDE LAYERS

(*a*) *Features observed in cross sections.* The microstructures, morphologies, and preferred growth orientations of the Fe sulfide scales vary with temperature and $H_2S/H_2$ ratio. Figure 3 shows typical microstructures and morphologies for sulfide layers formed at 778 K in ~1000 ppmv $H_2S$. After 5 hr the sulfide totally covers the metal surface (Fig. 3a). As the reaction proceeds, the metal retreats from the sulfide layer creating void space (Fig. 3b, 3c). The sulfide layer plastically deforms into the newly created void space to maintain contact with the metal. When the iron sulfide reaches its deformation limit, it cracks and gas penetrates to the metal–sulfide interface. Finer grained, randomly oriented crystals then grow between the metal and original sulfide scale leading to two distinct sulfide layers (Fig. 3d). The outer layer contains larger, compact, uniformly oriented crystals separated by transverse cracks and the inner layer contains smaller, randomly oriented crystals with a large amount of void space. The two layers are separated by long longitudinal cracks. The brittle outer layer easily breaks away from the sample during handling. In contrast, the inner layer adheres strongly to the metal.

Sulfidation of iron metal frequently, but not exclusively, leads to the formation of two sulfide layers. Figure 4a shows a sample formed in ~100 ppmv $H_2S$ at 673 K. The unbroken sulfide layer is in continuous contact with the metal and has no visible void space. However, the metal surface is very rough and jagged. Figure 4b shows a blistered sulfide layer. A second sulfide layer formed under the blister and merged with the original layer. The inner layer is half as thick as the outer layer. Figure 4c shows two thick, well developed sulfide layers. The outer sulfide layer detached from the metal surface after a relatively low extent of reaction.

Some conditions lead to formation of sulfide layers that slide off from the metal surface as thin, cohesive sheets that remain intact as long as they are not handled roughly. Optical microscopy and XRD patterns of the inner and outer surfaces of some of these layers show large, uniformly oriented crystals on the outer sides and smaller, randomly oriented crystals on the inner sides. Figure 4d shows three thin, compact sulfide layers with very little cracking. This suggests that the growth and rapid removal of thin layers from the metal surface leads to these multilayer structures and that the layers do not deform towards the retreating metal interface. This growth behavior allows almost continuous contact between the gas and metal. As a result, linear growth kinetics are observed even after long reaction times.

Figure 4e shows a sulfur rich pyrrhotite (~$Fe_{0.90}S$) with a large amount of vertical cracking characteristic of this phase (e.g., Fig. 4 of Fegley *et al.* 1995). This sample formed at a relatively high sulfur fugacity, and its composition agrees with thermodynamic predictions. Figure 4f illustrates a good example of the distinct two layer structure with noticeably different crystal sizes and orientations. However, the inner layer is much thicker than that shown in Fig. 3d. Apparently, transverse cracks formed in this sample at a much earlier stage of the reaction and led to the formation of a large inner layer at the expense of the outer one. In fact, a large range of both inner and outer layer thickness were observed in our experimental samples. The formation of the inner layer is dependent on the timing of the fracture of the outer sulfide layer.

Figures 4g and 4h show two samples with large, but drastically different sulfide layers. The sample in Fig. 4g was heated for 90 min at 1173 K in an ~10,000 ppmv $H_2S$ gas mixture. About 55% of the iron metal reacted to form large, uniformly oriented sulfide crystals. The absence of a well developed inner layer suggests that transverse cracking did not occur until the later stages of reaction. In contrast, the sample in Fig. 4h was heated in ~10,000 ppmv $H_2S$ at 923 K for 18.5 hours. About 80% of the iron metal reacted during heating. The outer sulfide layer is noticeably different than that shown in Fig. 4g. The sulfide crystals are not as blocky and straight edged and an inner sulfide layer has formed.

Observations of two distinct crystal layers, of transverse

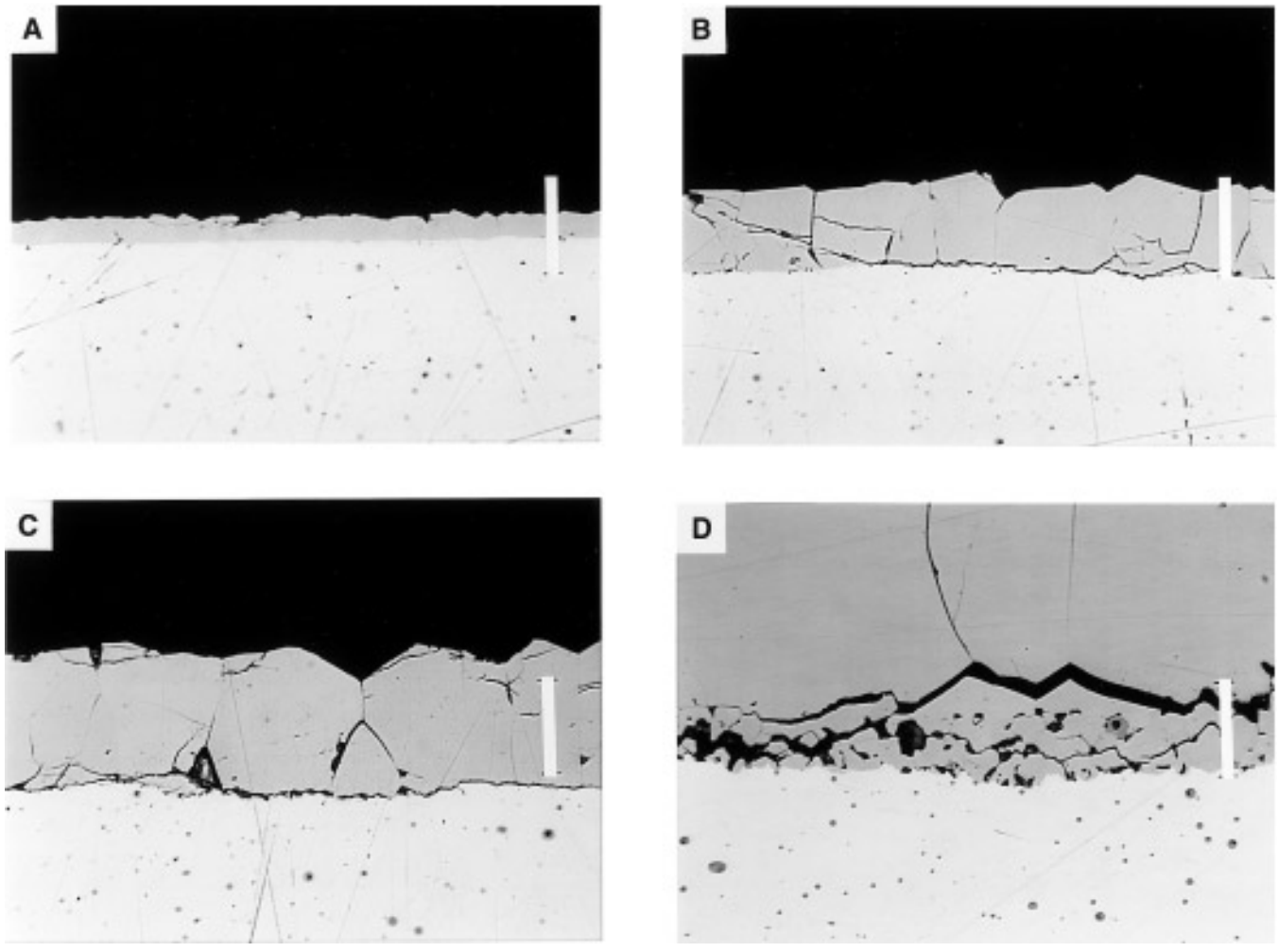


**FIG. 3.** Reflected light photomicrographs illustrating variations of sulfide layer morphology with increasing reaction time. All samples were formed in ~1,000 ppm $H_2S$ at 778 K. Reaction times are 5, 24, 48, and 450 hr for a, b, c, and d respectively. Each scale bar corresponds to 32 $\mu$m.

and longitudinal cracks, and of subsequent crystal growth at the metal surface were also reported by metallurgists who studied FeS formation in S vapor and $H_2S$–$H_2$ mixtures (see Table IV and Young 1980). Thin paper-like sulfide layers that easily detached from the metal were also observed by Orchard and Young (1989) during reactions of $H_2S$–$H_2$ mixtures with Fe-Ni alloys. However, to our knowledge, the formation of multiple smooth layers has not been reported previously.

(*b*) *Porosity measurements.* We measured the porosity of the sulfide layers by plotting their thickness versus half of the thickness change of the iron metal (Fig. 5). This could be done for 60 of the 95 total samples. Assuming that the area of the sample remained constant throughout the reaction, the change in thickness is due to the increase in volume from the conversion of Fe to FeS plus void space. Ideally, the ratio of the two thicknesses should be equal to the ratio of the molar volumes ($M_v$) of the two phases ($M_{v,FeS}/M_{v,Fe} = 18.20\ cm^3/7.09\ cm^3 = 2.57$). A larger value is due to porosity within the sulfide layer. The slope of the line in Fig. 5 gives the average molar volume ratio of all the sulfide layers used in the regression. A least-squares analysis yields

$$th_{sulfide} = 2.78(\pm 0.08)th_{Fe} - 0.000(\pm 0.001), \qquad (3)$$

corresponding to a mean porosity of ~8 ± 3%. The void space between the inner and outer sulfide layers probably accounts for most of this porosity.

(*c*) *Surface features.* Figure 6 illustrates the range of surface features observed on the Fe sulfide layers. Abundant small crystals growing in the striations of the iron metal are commonly observed on samples reacted for short times (Fig. 6a). The patchy sulfide growth is due to Fe sulfide nucleation at high energy regions where imperfections are present on the Fe metal surface. As the reaction

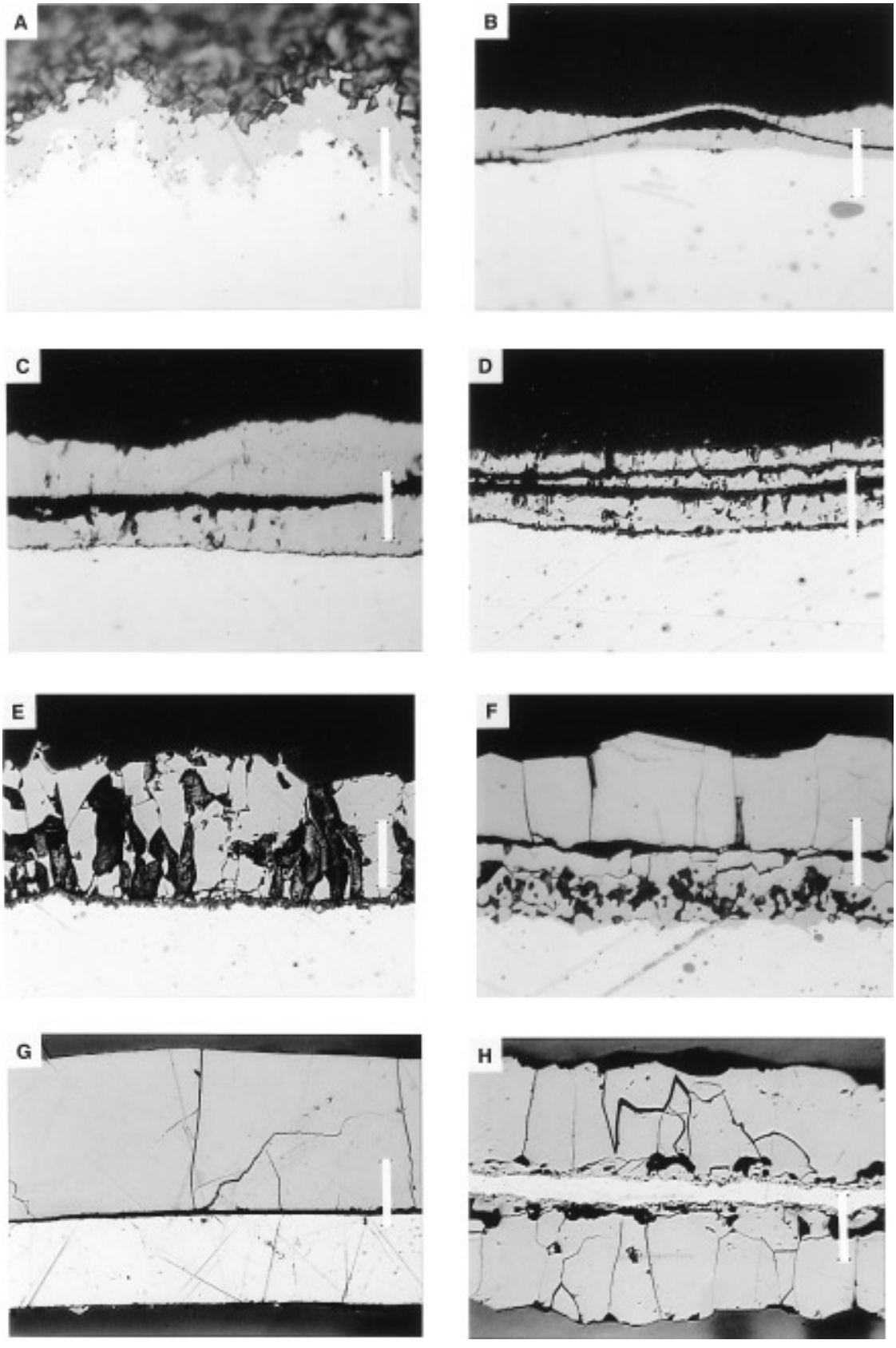


**FIG. 4.** Reflected light photomicrographs illustrating other observed variations in sulfide layer morphology. (a) Sample 31, formed in ~100 ppm $H_2S$ at 673 K and reacted for 102 hr. (b) Sample 91, formed in ~10,000 ppm $H_2S$ at 558 K after 18.5 hr. (c) Sample 43, formed in ~50 ppm $H_2S$ at 616 K after 74.5 hr. (d) Sample 46, formed in ~50 ppm $H_2S$ at 614 K after 222 hr. (e) Sample 108, formed in ~10,000 ppm $H_2S$ at 673 K after 118 hr. (f) Sample 15, formed in ~1,000 ppm $H_2S$ at 851 K after 35 hr. The scale bar in (a)–(f) corresponds to 20 $\mu$m. (g) Sample 86, formed in ~10,000 ppm at 1173 K after 1.5 hr. Scale bar = 80 $\mu$m. (h) Sample 93, formed in ~10,000 ppm $H_2S$ at 923 K after 18.5 hr. Scale bar = 160 $\mu$m. See Text for discussion of features.

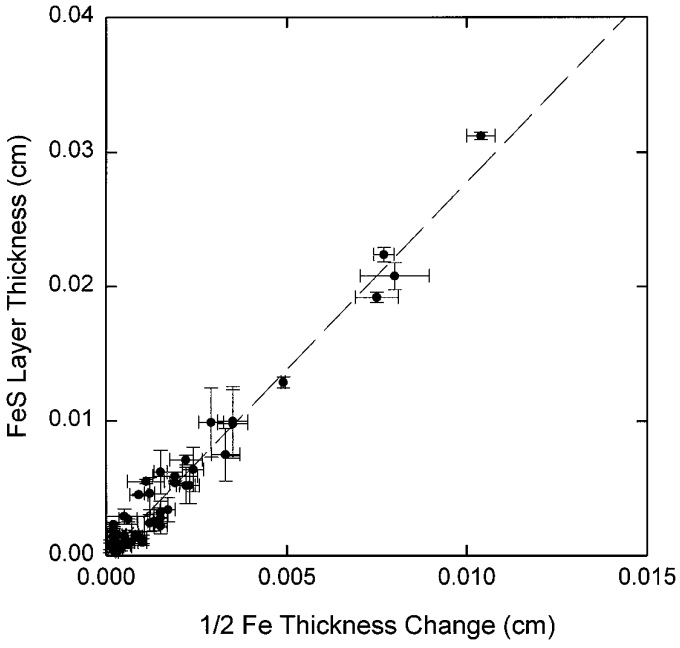


**FIG. 5.** Determination of sulfide layer porosity by comparison of the measured sulfide layer thickness to the amount of Fe reacted. The slope is the ratio of molar volumes of FeS and Fe. The least-squares fit to the data gives a calculated slope of 2.78 ± 0.08 indicating a porosity of 8 ± 3% for the FeS layers.

progresses the patchy regions grow together and small crystals cover the entire surface of the metal. The crystals grow with time and distinct features are visible on larger crystals. The majority of the crystals appear rounded, while others are acicular, or rectangular and blocky with sharp angles and smooth faces, and some have rough, striated surfaces (Fig. 6b). Close examination of very large crystals reveals a thin skin $<1$ $\mu$m thick on the crystals (Fig. 6c). Energy dispersive spectrum (EDS) analyses show a large amount of sulfur in this skin relative to the FeS crystals. Young (1980) reported the formation of thin layers of pyrite at the outer edge of FeS layers formed under similar conditions, consistent with our EDS data.

The sulfide grains are well developed and frequently show 120° triple junctions (Fig. 6b). Very little porosity is evident and pores are mainly found inside grains and not at grain boundaries. Hexagonal plate-like steps are also commonly observed on the grain surfaces (Fig. 6d). Similar steps were also observed by Jamin-Changeart and Talbot-Besnard (1965) and by Narita and Nishida (1973a). The latter authors noted that the steps imply screw dislocations inside the sulfide grains. These steps are also observed in lunar troilites that have apparently grown by vapor-solid reactions (e.g., Frondel 1975, Fig. 2.2). Narita and Nishida (1973a) reported that the growth steps disappeared as the sulfur fugacity decreased. We observed hexagonal growth steps only in sulfides formed in ~1,000 ppmv $H_2S$ mixtures.

## X-RAY DIFFRACTION RESULTS

(*a*) *Growth orientations.* XRD patterns of samples formed under various experimental conditions are shown in Fig. 7. In the majority of cases, the pattern is dominated by a single peak because the sulfide crystals at the outer surface of the sulfide layer are uniformly oriented along a crystallographic plane. However, the crystal orientation is not the same for all the sulfide layers but varies with reaction conditions. The variation in preferred growth orientation apparently affects the rate of FeS formation. A decrease in the reaction rate between 613 K and 643 K in 50 ppmv $H_2S$ correlates with a change in crystal orientation (Fig. 7). The change in growth orientation of sulfide layers was reported by other groups (Narita and Nishida 1973a; Fryt *et al.* 1979b) but the underlying reasons are not well understood (Young 1980).

(*b*) *Fe/S ratios.* The Fe/S atomic ratios of the sulfides were calculated from the mean $d(102)$ spacings using the equation given by Yund and Hall (1969):

$$\text{Atom-\% Fe} = 45.212 + 72.86(d_{102} - 2.0400) + 311.5(d_{102} - 2.0400)^2 \quad (4)$$

We also checked Eq. (4) by fitting our own parabolic equation to the hexagonal pyrrhotite and troilite $d(102)$ spacings given by Arnold (1962), Toulmin and Barton (1964), and Fleet (1968). The calculated atomic percentages for Fe agreed with those calculated from equation (4) within the $2\sigma$ uncertainty of ±0.13% (Yund and Hall, 1969).

Table III lists all Fe/S ratios determined by XRD. The mean $1\sigma$ uncertainties on the Fe/S ratios range from ±0.9% for XRD powder patterns measured with silicon powder as an internal standard to ±2.0% for XRD patterns measured by placing the entire sample into the diffractometer. We compare these observed Fe/S ratios with those obtained from other methods and with predictions from chemical equilibrium calculations.

(*c*) *Cell parameters.* In samples that produced enough material to obtain an XRD powder pattern, cell parameters were determined using the program MICRO-CELLREF from MDI. Various pyrrhotite unit cells were refined by least squares techniques employing the Apple-NBS code (Evans *et al.* 1973). The troilite unit cell($3^{1/2}A$ $2C$) gave the best fit in all cases except for sample 107, where the $5C$ pyrrhotite superstructure provided the best fit. The latter result is consistent with the Fe/S ratio of 0.92 for sample 107. In Fig. 8 we plot the length of the $C$ axis of the NiAs unit cell versus the atomic percentage of sulfur.

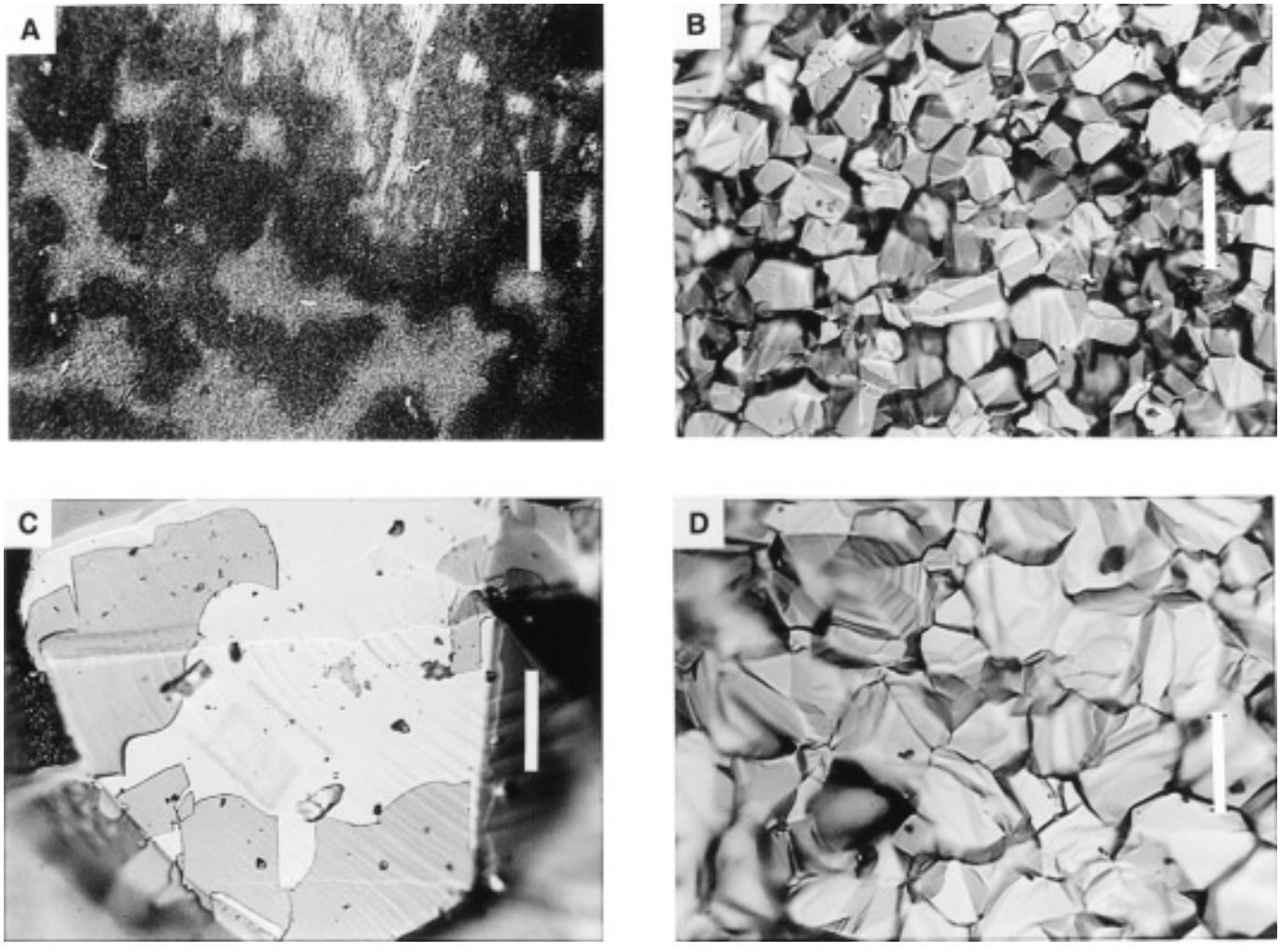


**FIG. 6.** Reflected light photomicrographs of several surface microstructure features. (a) Sample 91, formed in ~10,000 ppm $H_2S$ at 558 K. Patches of sulfide crystals are visible. The metal surface is not entirely covered and bare iron is still visible in the upper right corner of the photograph. Scale bar = 80 $\mu$m. (b) Sample 59, formed in ~1,000 ppm $H_2S$ at 673 K. Several 120° triple junctions are visible. In (b)–(d) scale bar = 32 $\mu$m. (c) Sample 98, formed in ~10,000 ppm $H_2S$ at 923 K. A thin (~1 $\mu$m) skin covers a large sulfide crystal. Steps on the surface of the crystal are apparent. (d) Sample 15, formed in ~1,000 ppm $H_2S$ at 851 K. Hexagonal steps are visible in upper left corner of photo.

Data from Turkdogan (1968) and Haraldsen (1941) are also shown. Turkdogan (1968) reported that the troilite unit cell accommodates sulfide compositions ranging from Fe/S ~ 0.98 to Fe/S ~ 1. This is consistent with our results that samples ranging in composition from Fe/S = 0.984 to 1.007 have the troilite unit cell.

## ELECTRON MICROPROBE RESULTS

(*a*) *Fe/S ratios.* The bulk compositions of the sulfide layers were determined by averaging multiple electron microprobe analyses of each layer. The Fe/S ratios for individual samples are listed in Table III. The mean Fe/S ratios for all sulfide layers produced in the same gas mixture along an isotherm are listed in Table V. The mean $1\sigma$ uncertainty on the Fe/S ratios is $\pm 1.5\%$.

We checked the electron microprobe analyses of our samples by analyzing natural troilites from the Staunton octahedrite, two LL3 chondrites (Y-790519 and ALH-764), and a lunar sample (67513, 7012). The natural troilites have Fe/S ratios ranging from ~0.98 to ~1.01 with typical $1\sigma$ uncertainties of $\pm 1$–2%. The analyses with Fe/S >1.00 possibly include contributions from buried or neighboring Fe grains in the meteorite sections. The electron microprobe analyses of natural troilites and synthetic sulfides give the same range of Fe/S ratios (excluding the experimental samples predicted to be hexagonal pyrrhotite instead of troilite).

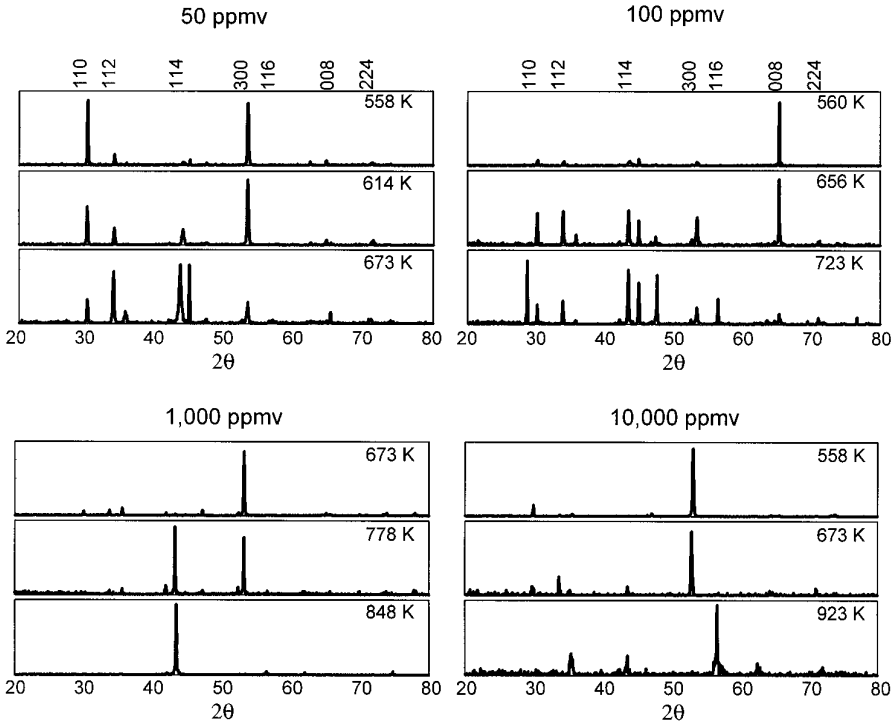


**FIG. 7.** Representative XRD patterns of Fe sulfides for various experimental conditions. Miller indices of each peak position in the troilite pattern are labeled at the top of the two columns. A single high intensity peak indicates preferential growth along a specific crystallographic axis. Crystal orientation varies with both gas composition and temperature of reaction. The reason for the variations are not well understood (e.g., Young 1980).

(*b*) *Traverses across layers.* Electron microprobe traverses were made across sulfide layers to determine whether or not any compositional variations were present. Step sizes of 5–10 $\mu$m were used. The analytical results are shown in Fig. 9 (~1000 ppmv $H_2S$) and in Fig. 10 (~10,000 ppmv $H_2S$). The Fe/S atomic ratios are plotted versus $x/x_t$, where $x_t$ is the total thickness from the metal-sulfide interface. No traverses could be made for sulfide layers formed in the 25, 50, and ~100 ppmv $H_2S$ mixtures because the layers were ≤5–10 $\mu$m thick.

The high Fe/S ratios measured close to the Fe–FeS boundary are probably due to boundary fluorescence of the nearby unreacted metal. Most layers show a decreasing Fe/S ratio and hence an increasing sulfur content toward the outer edge of the sulfide layer. This occurs continuously (samples 62, 67, 70, 96, 97) or suddenly at the end of the layer (samples 61, 63, 65, 68, 80, 81, 93). Narita and Nishida (1973b) reported similar variations in sulfur content in FeS formed on pure Fe at 973 K under various sulfur pressures.

The observed decrease of the Fe/S ratio across the sulfide layers is explained by considering equilibrium at each interface (Wagner 1951). The composition of the sulfide at the metal–sulfide interface is fixed at Fe/S = 1 by the presence of the Fe metal. However, the outer edge of the sulfide layer is in equilibrium with the external $H_2S$–$H_2$ atmosphere, which generally has a higher sulfur fugacity ($f_{S_2}$) than that fixed by the metal-sulfide boundary. Thus, the outer edge of the sulfide should be more sulfur rich and have a lower Fe/S ratio. We return to this point later when discussing the kinetics of sulfide layer formation.

## GRAVIMETRIC ANALYSES BY COMBUSTION

For samples where enough sulfide was produced, the sulfides were analyzed gravimetrically by heating the powder in air at temperatures up to 1100°C for several days to form hematite (verified by XRD). The Fe/S ratio in the starting material was calculated from the observed weight loss. Depending on the amount of material available for combustion and the accuracy of weighing, this method gives very accurate and precise determinations of the Fe/S ratio in an Fe sulfide. By using this method, Condit *et al.* (1974) determined Fe/S ratios in pyrrhotite to ±0.2% and Fegley *et al.* (1995) found that Fe/S ratios in pyrite could be determined to ±0.02%. The results of the gravimetric analyses are listed in Table V and plotted in Fig. 11.

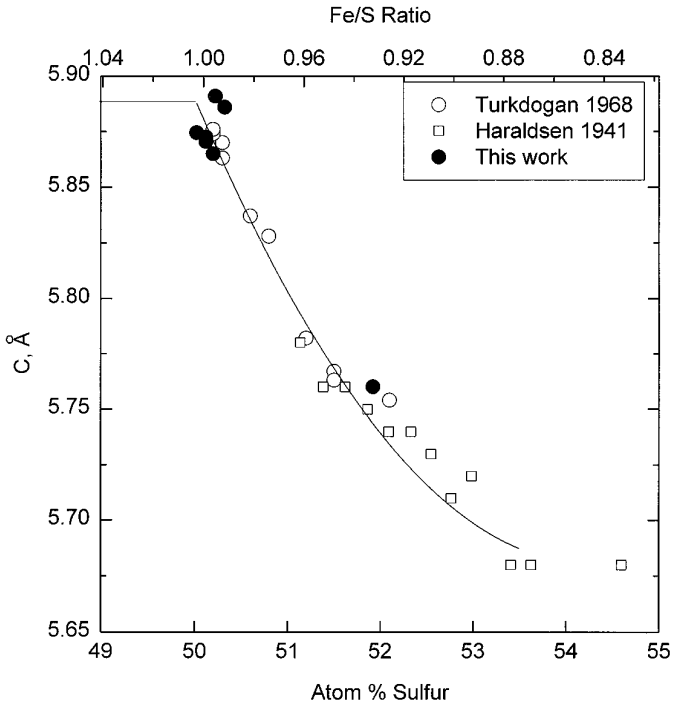


**FIG. 8.** A plot of the variation in the *C*-axis of the NiAs unit cell as a function of atomic % sulfur. The Fe/S ratio is also plotted along the top axis. Data from Turkdogan (1968) and Haraldsen (1941) are shown for comparison. The solid line (from Turkdogan 1968) is the variation in the NiAs unit cell with sulfur content. Our data (solid circles) cluster near the predicted value for the troilite unit cell. The point near 52 atomic % sulfur is hexagonal pyrrhotite (see text for further discussion).

## COMPARISON OF PREDICTED AND OBSERVED Fe/S RATIOS

Table V and Fig. 11 present the Fe/S ratios determined by XRD, electron microprobe analyses, and gravimetric analyses. The Fe/S ratios from the three independent data sets agree well with each other. The Fe/S ratios determined gravimetrically typically have $1\sigma$ uncertainties of $\pm 0.4\%$, while the typical $1\sigma$ uncertainties are $\pm 0.9\%$ for XRD powder patterns, $\pm 2.0\%$ for XRD layer patterns and $\pm 1.5\%$ for the electron microprobe analyses. Condit *et al.* (1974) reported average uncertainties of $\pm 1\%$ in Fe/S ratios determined by XRD and $\pm 0.2\%$ in Fe/S ratios determined gravimetrically. We also compared the Fe/S ratios determined by different techniques on individual samples. This comparison shows that there are no systematic errors between the three techniques because the mean differences (and $1\sigma$ errors) are $0.3\% \pm 2.0\%$ (XRD–microprobe), $0.3\% \pm 0.4\%$ (XRD–combustion), and $-0.3\% \pm 0.6\%$ (microprobe–combustion).

Figure 11 compares the observed Fe/S ratios to those predicted by gas–solid equilibrium between $Fe_{1-\delta}S$ and a gas of known sulfur fugacity (e.g., an $H_2S$–$H_2$ gas mixture). The dependence of the Fe/S ratio of $Fe_{1-\delta}S$ upon the temperature and sulfur fugacity is well known (Barker and Parks 1986; Burgmann *et al.* 1968; Nagamori and Kumeda 1968; Niwa and Wada 1961; Rau 1976; Rosenquist 1954; Toulmin and Barton 1964; Turkdogan 1968). Hägg and Sucksdorff (1933) showed that the Fe deficiency is due to Fe vacancies in the lattice. Libowitz (1972) interpreted the experimental studies of $Fe_{1-\delta}S$ stoichiometry in terms of Fe vacancy formation.

Sulfur exchange between $Fe_{1-\delta}S$ and a gas phase (e.g., either sulfur vapor or an $H_2S$–$H_2$ mixture) occurs via the reaction

$$\tfrac{1}{2}S_2\,(g) = S_s + V''_{Fe} + 2h^{\cdot} \qquad (5)$$

which preserves mass, charge, and site balance. Equation (5) is written in Kröger–Vink notation in which the general convention $S_P^C$ is used to represent a species S with charge C at crystallographic position P (e.g., see Schmalzried 1974; Kingery *et al.* 1976). Equation (5) shows that incorporation of a sulfur atom on a sulfur site ($S_S$) in $Fe_{1-\delta}S$ also leads to the formation of an Fe vacancy with a $-2$ charge ($V''_{Fe}$) and of two electron holes which each have a $+1$ charge ($h^{\cdot}$).

Libowitz (1972) derived equations which quantitatively relate the Fe vacancy concentration ($\delta$) to the sulfur fugacity ($f_{S_2}$). Rau (1976) subsequently made more precise measurements of iron sulfide stoichiometry as a function of $T$ and $f_{S_2}$ and revised Libowitz's numerical constants. Rau's equations were used to calculate the gas–phase equilibrium line for $Fe_{1-\delta}S$ in Fig. 11.

The comparison in Fig. 11 shows generally good agreement between the observed and predicted Fe/S ratios (no data are available yet for the 25 ppm samples). Most of the observed compositions fall on the theoretical curve. The observed Fe/S ratios decrease with decreasing temperature as predicted. However, the lower temperature sulfides in the 50 and 100 ppmv experiments display Fe/S ratios significantly lower than predicted. These discrepancies are possibly due to incomplete equilibrium with the $H_2S$–$H_2$ gas (e.g., see Turkdogan 1968). On the other hand, the analytical data in Table III for individual samples along an isotherm do not show a clear trend with time (outside the 1.5–2.0% $1\sigma$ uncertainties of the microprobe and XRD data).

The other discrepancy between the observed and predicted data occurs for some sulfides formed at 558 K in 10,000 ppmv $H_2S$ mixtures. Figure 11 shows two different sets of Fe/S analyses for these conditions. The sulfides which formed at shorter run times have a mean Fe/S ratio = 0.99. In contrast, the sulfides which formed over longer run times have a mean Fe/S ratio = 0.92. The predicted Fe/S ratio = 0.95 is between these sets of observed

values. XRD shows that the more Fe-rich sulfides are hexagonal pyrrhotite.

Finally, we discuss the Fe/S ratio of troilite. Because there is a finite concentration of lattice defects in any crystal which is not at absolute zero, the Fe/S ratio of troilite is not equal to unity. Furthermore, because the concentration of various types of defects is a function of the temperature and the sulfur fugacity (e.g., Libowitz 1972; Rau 1976) the Fe/S ratio of troilite should also vary with these parameters. In fact, Libowitz (1972) calculated defect concentrations varying from 0.15% (Fe/S = 0.9985) at 973 K to 1.04% at 1373 K. Similar variations are predicted from Rau's (1976) equations mentioned earlier. In this regard we note that the predicted variation in the Fe/S ratio of troilite could be used as a mineralogical thermometer to measure sulfide equilibration temperatures in meteorites.

Experimental determination of the Fe/S ratio in troilite have been done by several groups. Rosenquist (1954) reported Fe/S =1.002, Turkdogan (1968) gave Fe/S = 0.992, Condit *et al.* (1974) report Fe/S = 0.997, and Horwood *et al.* (1976) give Fe/S = 0.996. Our own XRD results give Fe/S = 1.007–1.012 for the most Fe-rich troilites produced in our experiments (samples 27, 29, 35, and 39 in Table III). However, within the uncertainty (±0.9–2.0%) of our XRD data, these samples have Fe/S = 1.000. The XRD data of other investigators also have an uncertainty of ±1% (e.g., Condit *et al.* 1974), so the reported deviations from unity may not be significant. Nevertheless, careful gravimetric analyses may be able to resolve this question.

## KINETICS AND MECHANISM OF IRON SULFIDE FORMATION

(*a*) *Kinetic data.* Two independent methods were used to measure the extent of reaction as a function of time. In the gravimetric method, the fraction of Fe reacted ($\alpha$) in the samples was calculated from the observed weight gain. Iron sulfide formation occurs via the reaction

$$H_2S(g) + (1 - \delta)Fe(s) \rightarrow Fe_{1-\delta}S(s) + H_2(g), \quad (1)$$

and the composition of each sulfide sample was determined by one or more analytical methods (XRD, electron microprobe, combustion). The fraction of Fe reacted ($\alpha$) was then calculated as

$$\alpha = (1 - \delta) f_{st} \frac{\Delta w}{w_i}, \quad (6)$$

**TABLE V**
**Effects of Temperature and Gas Composition on Fe/S Ratio of Iron Sulfide Layers**

| Temp | ppm | Observed Fe/S atomic ratio | | | | Gas-Solid |
|---|---|---|---|---|---|---|
| (K) | $H_2S$ | XRD[a] | Microprobe[a] | Combustion[a,b] | Mean | Equilibrium |
| 558 | 50 | 0.956 | 0.962 | n.a. | 0.959 | 0.994 |
| 613 | 50 | 0.957 | 0.949 | n.a. | 0.953 | 0.997 |
| 673 | 50 | 0.988 | 0.982 | n.a. | 0.985 | 0.998 |
| 558 | 100 | 0.972 | 0.988 | n.a. | 0.980 | 0.991 |
| 658 | 100 | 0.997 | 0.996 | n.a. | 0.997 | 0.996 |
| 723 | 100 | 1.004 | 0.965 | n.a. | 0.985 | 0.998 |
| 673 | 850 | 0.990 | 0.986 | n.a. | 0.988 | 0.987 |
| 778 | 850 | 0.996 | 0.988 | 0.985 | 0.990 | 0.993 |
| 848 | 850 | 0.999 | 0.979 | 0.989 | 0.989 | 0.995 |
| 923 | 850 | 0.990 | 0.989 | 0.992 | 0.990 | 0.997 |
| 558 | 10800 | 0.926 | 0.967 | 0.936 | 0.943 | 0.954 |
| 673 | 10800 | 0.995 | 0.981 | 0.983 | 0.986 | 0.965 |
| 923 | 10800 | 0.987 | 0.979 | 0.988 | 0.985 | 0.988 |
| 1173 | 10800 | 0.991 | 0.983 | 0.991 | 0.988 | 0.992 |

[a] Uncertainties on XRD, microprobe, and combustion are ±0.9–2.0%, 1.5%, and 0.4%, respectively.

[b] Combustion data are for samples 53, 54, 60, 86, 98, 109, and 110.

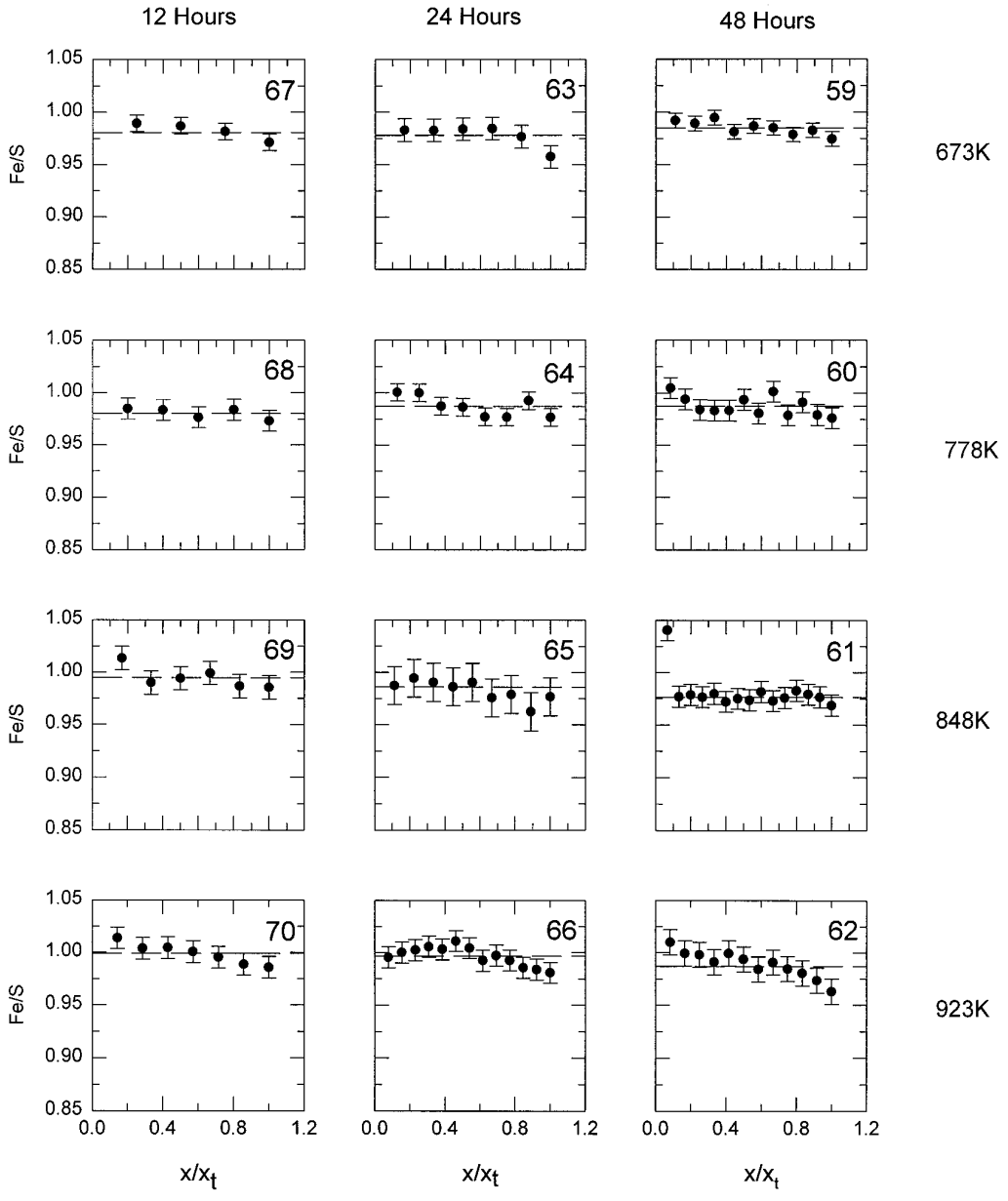


**FIG. 9.** Representative electron microprobe traverses across sulfide layers formed in ~1,000 ppm $H_2S$. The corresponding sample number is located in the upper right corner of each plot. Normalized distance (distance from metal/total layer thickness) is plotted on the *x*-axis. The sulfide composition (Fe/S ratio) is plotted on the y-axis and ranges from 0.85 to 1.05. The dashed horizontal line represents the average of all points in the traverse. Error bars represent $1\sigma$ uncertainties.

where $\Delta w$ is the weight gain, $w_i$ is the initial weight of the Fe, and $f_{st} = 1.742$ is a stoichiometric factor from the mass balance of Eq. (1). The term $(1 - \delta)$ in Eq. (6) is calculated from the analytical data. The $\alpha$ values calculated from Eq. (6) have typical uncertainties ($1\sigma$) of ±2% due to uncertainties in the stoichiometry and weight of the samples.

In the geometric method, $\alpha$ was calculated from the fractional thickness change of the Fe metal in the samples. The equation used is

$$\alpha = \left(1 - \frac{C_t}{C_0}\right), \tag{7}$$

where $C_0$ is the initial thickness of the Fe foil and $C_t$ is the thickness of the remaining Fe metal after reaction for some time $t$. The initial thickness of the Fe foils was measured with a micrometer. The thickness of the remaining Fe metal ($C_t$) in the cross-sections of the samples was measured with an optical microscope. The $\alpha$ values calculated from Eq.

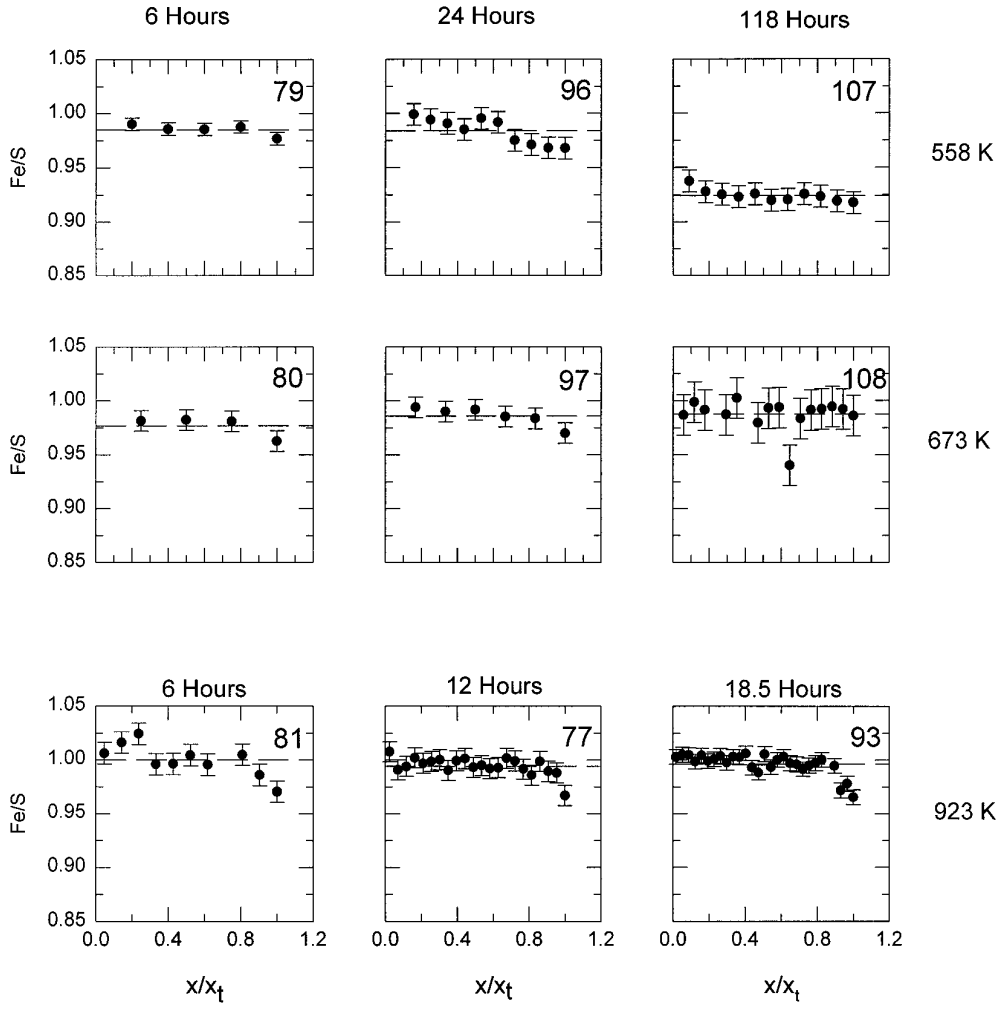


**FIG. 10.** Representative electron microprobe traverses across sulfide layers formed in ~10,000 ppm $H_2S$. A drastic change in composition occurs between 48 and 72 hr in samples that form along the 558 K isotherm. The axes are the same as described in the caption for Fig. 9.

(7) have typical uncertainties ($1\sigma$) of ±3% due to the measurement uncertainties.

Figure 12 illustrates the excellent agreement between the two methods. An unweighted linear least-squares fit to the 60 data points in Fig. 12 gives

$$\alpha_{\text{geometric}} = 0.01(\pm 0.04) + 0.99(\pm 0.02)\alpha_{\text{gravimetric}} \quad (8)$$

which within uncertainty is the same as an 1:1 diagonal. Table III lists the gravimetric and geometric $\alpha$ values for the experimental samples. Geometric data were obtained for 60 of the 95 samples. Measurements were not obtained for the other 35 samples because the layers were either too thin or were lost during sample polishing and mounting. Therefore, we used the gravimetric data to determine the rate laws and their dependence on temperature and $H_2S/H_2$ ratio.

(*b*) *Rate Laws.* Gas–solid reactions, such as the oxidation and tarnishing of metal, follow a variety of different rate laws depending upon the type of metal, the time period of reaction, the reactive gas partial pressure, and the rate controlling mechanism (e.g., see Schmalzried 1974). Our data show that Fe sulfide formation follows both linear and parabolic kinetics under the conditions studied.

Linear and parabolic rate laws were distinguished by plotting the reaction progress (weight gain per $cm^2$ sample area) versus time. Straight lines indicate linear kinetics and the slope gives the linear rate constant $k_l$,

$$(\Delta w/A) = k_l t \quad (9)$$

In Eq. (9), $\Delta w$ is the weight gain, $A$ is the sample area in $cm^2$, $t$ is time in hours, and $k_l$ has units of g $cm^{-2}$ $hr^{-1}$. Linear kinetics are displayed during the early stages of tarnishing reactions when the supply of gas molecules, adsorption or chemical reactions at the solid–gas interface control the overall rate of reaction.

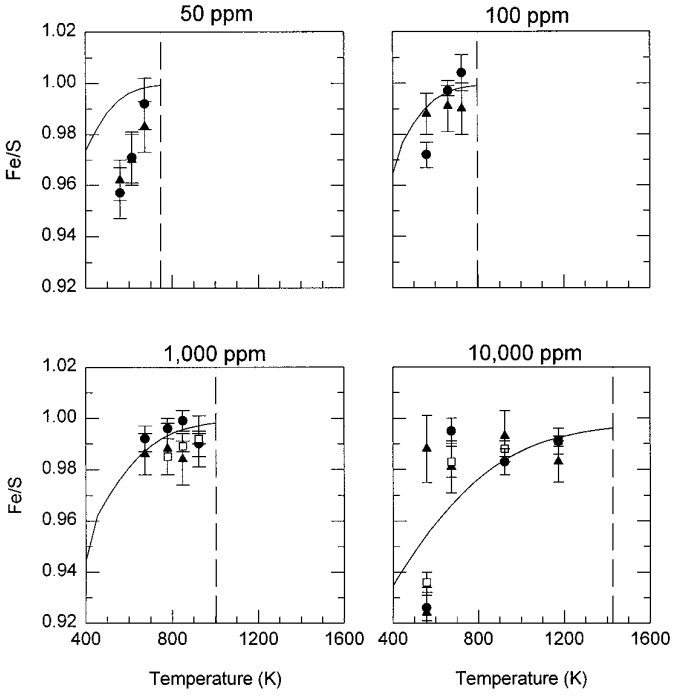


**FIG. 11.** A plot of the Fe/S ratios for sulfides formed under four different $H_2S$ gas concentrations (nominally 50, 100, 1,000, and 10,000 ppm) as a function of temperature. The solid curve is the predicted variation in the Fe/S ratio derived from equations in Rau (1976). The dashed vertical line represents the condensation temperature of FeS. The solid circles represent our XRD data, the solid triangles our electron microprobe data, and the open squares our combustion data. The $1\sigma$ uncertainties for each technique are also shown.

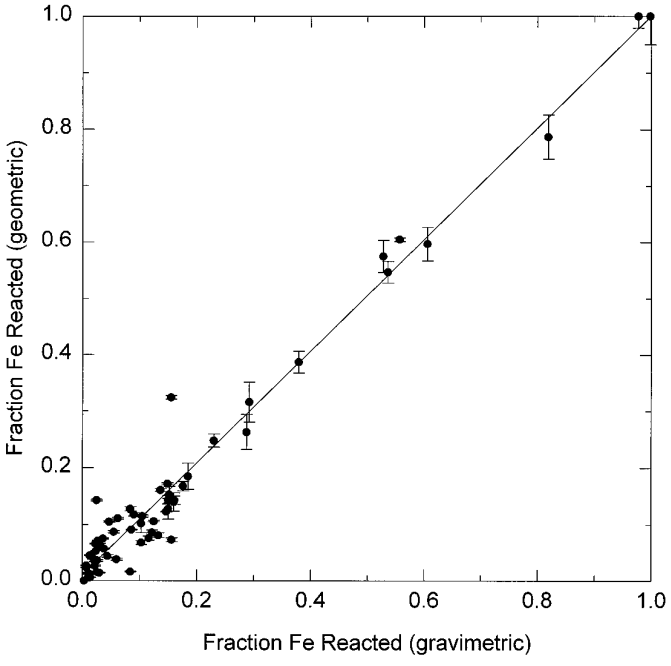


**FIG. 12.** A plot comparing the fraction of Fe reacted, calculated by two independent methods (gravimetric and geometric). The solid line is a least-squares linear regression for 60 data points. Error bars are $1\sigma$ uncertainties. The error bars for the gravimetric data are smaller than the plotted data points.

When the scale layer reaches a critical thickness, the rate of diffusion of $Fe^{2+}$ through the product layer becomes slower than the rate of the chemical reaction at the sulfide–gas interface (Wagner 1951; Schmalzried 1974). The chemical potential gradient across the sulfide layer is the driving force for the $Fe^{2+}$ ionic diffusion and this gradient is inversely proportional to the product layer thickness. Thus, in this case the rate law is expressed as

$$(\Delta w/A)^2 = k_p t, \qquad (10)$$

where $k_p$ is the parabolic rate constant with units of $g^2$ $cm^{-4}$ $hr^{-1}$. As Eq. (10) shows, plots of reaction progress versus time give parabolic curves. Equivalently, plotting $(\Delta w/A)^2$ vs time or $(\Delta w/A)$ vs time$^{1/2}$ yields straight lines with slope $k_p$. The relationship of the linear and parabolic rate laws to the mechanisms for iron sulfide formation are discussed later.

Figures 13–14 show that all the experiments in the ~50 and ~100 ppmv $H_2S$ gas mixtures followed linear kinetics. This is also true for the samples that formed in the 25 ppmv $H_2S$ gas mixtures. The samples heated for shorter times have incompletely formed sulfide scales. However,

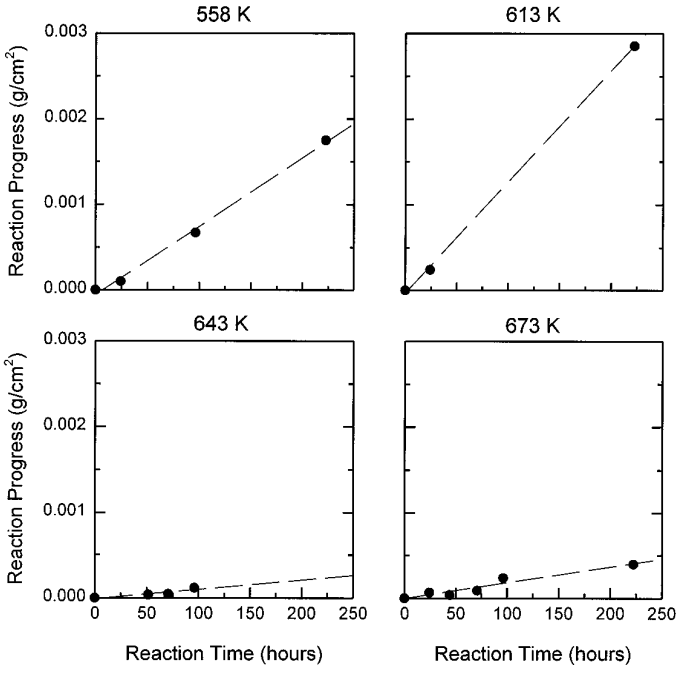


**FIG. 13.** Plots of reaction progress versus time along four isotherms (558, 613, 643, and 673 K) for samples formed in ~50 ppm $H_2S$. The dashed lines are linear least squares fits to the data. Linear kinetics are observed at all temperatures. A large increase in reaction rate occurs between 643 and 613 K and is potentially due to vacancy ordering in the sulfide at lower temperatures.

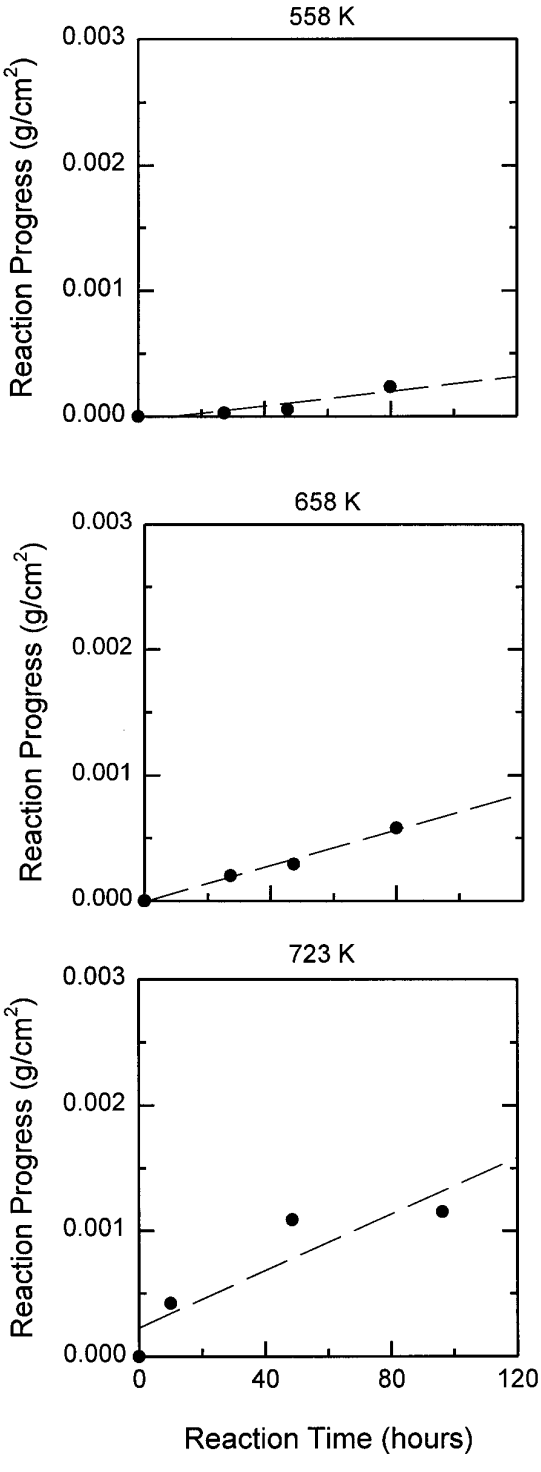


**FIG. 14.** Plots of reaction progress versus time along three isotherms (558, 658, and 723 K) for samples formed in ~100 ppm $H_2S$. The dashed lines are linear least-squares fit to data. All samples display linear kinetics.

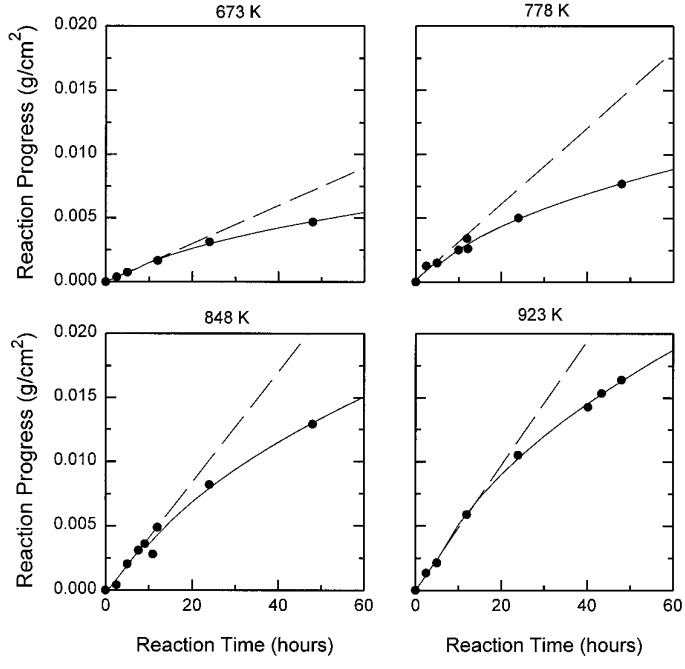


**FIG. 15.** Plots of reaction progress versus time along four isotherms (673, 778, 848, and 923 K) for samples formed in ~1,000 ppm $H_2S$. The dashed lines are linear least-squares fits to data points for experiments ≤10 hr. The solid curves are parabolic fits to longer reaction time experiments. Experiments at all temperatures show a transition from linear to parabolic kinetic behavior.

the samples heated for longer times are completely covered by compact and relatively non-porous sulfide layers. Because sulfide growth follows linear kinetics, the sulfide scales must be thinner than the critical thickness where diffusion becomes rate limiting.

Figure 15 shows the kinetic behavior for the ~1,000 ppmv $H_2S$ experiments where a transition from linear to parabolic kinetics is obvious. Optical microscopy (Fig. 3) reveals compact sulfide layers which do not have a large number of transverse cracks that extend down to the metal. These observations suggest that the gas did not have an easy pathway to the metal surface. The inner sulfide layers, which formed by gas penetration to the metal surface, are thinner and less developed than in samples where more cracks are observed in the initial sulfide layer.

The kinetic behavior of the samples formed in gas mixtures containing ~10,000 ppmv $H_2S$ (Fig. 16) varies with temperature. All sulfides formed at 923 K grew following parabolic kinetics. Iron sulfide formation is extremely rapid under these conditions and is complete within 24 hr. The scales are thick and compact with little or no development of an inner layer. At 558 K a transition from linear to parabolic kinetics occurs after 24 hr.

Linear kinetics that are somewhat erratic even for very long reaction times (146 hr) are observed for samples reacted at 673 K. This is due to the morphology of the layers on these samples. As discussed earlier, the sulfide layers lift off the metal surface during the course of the reaction.

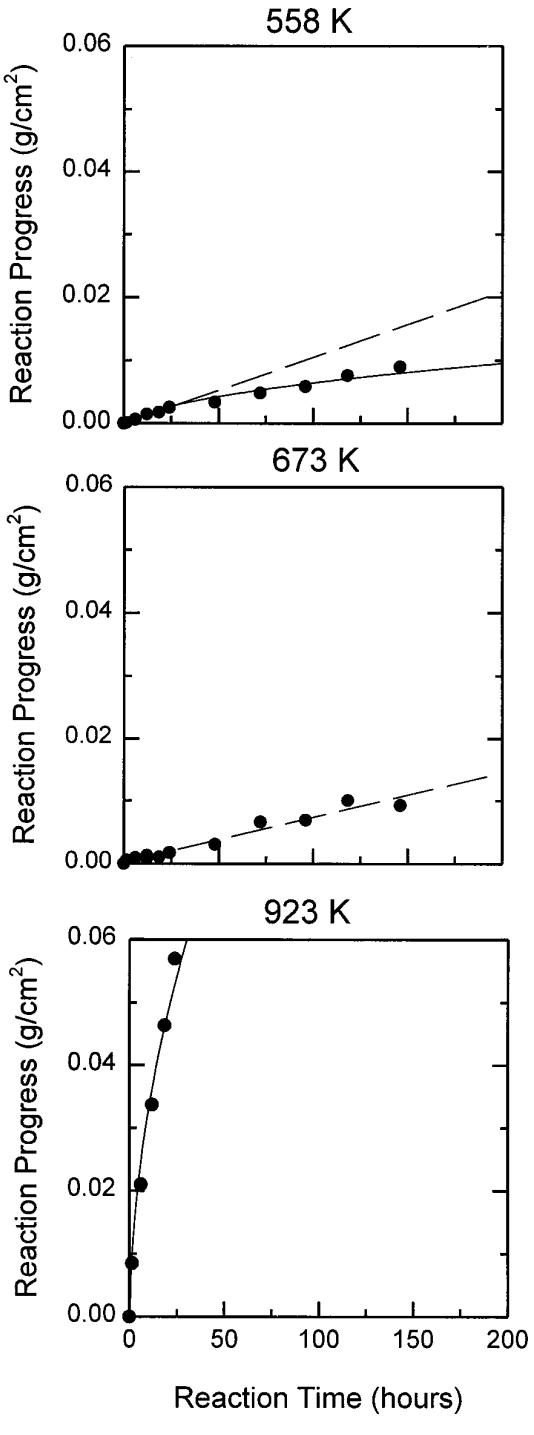


**FIG. 16.** Plots of reaction progress versus time along three isotherms (558, 673, and 923 K) for samples formed in ~10,000 ppm $H_2S$. The dashed lines are linear least-squares fits to data that display linear kinetics, while the solid curves are parabolic fits to data that display parabolic kinetic behavior. Samples formed at 923 K display only parabolic kinetics, while samples formed at 673 K display erratic linear kinetics. A transition from linear to parabolic kinetics were observed along the 558 K isotherm at approximately 25 hr.

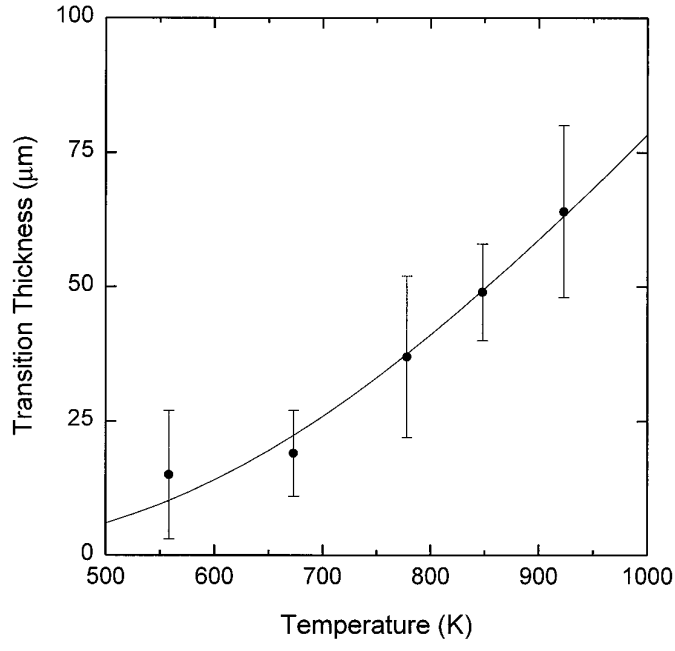


**FIG. 17.** A plot of the critical FeS layer thickness where the transition from linear to parabolic kinetics occurs as a function of temperature. The transition data points were determined graphically from data within Fig. 15 and 16 and then correlated with sulfide layer thickness measurements. The uncertainties are calculated from the range of sulfide thickness observed in samples near the transition regions. The solid line is an exponential function fit to the data.

This allows continuous contact between the gas and the metal and results in linear kinetic behavior. The stage at which the sulfide pulls away from the metal is somewhat arbitrary and therefore erratic kinetic behavior is observed under these conditions. Orchard and Young (1989) reported similar behavior for sulfide layers formed on iron-nickel alloys.

We used the data in Fig. 15–16 to estimate the critical scale thickness for the transition from linear to parabolic kinetics. All four of the isotherms studied in the ~1,000 ppmv $H_2S$ gas mixtures and one in 10,000 ppmv $H_2S$ show a transition from linear to parabolic kinetic behavior. We graphically determined the transition points and plot the corresponding layer thickness in Fig. 17. We fit the critical thickness ($t_{tr}$) data in Fig. 17 to the equation

$$t_{tr} = 1033(\pm 360)\ \exp[-2580(\pm 295)/T]\ \mu\text{m} \qquad (11)$$

because of an exponential dependence of reaction rates and diffusion coefficients on temperature.

(*c*) *Rate constants.* After establishing the rate laws, we calculated the appropriate linear or parabolic rate constant for each sample. These calculations used the $\alpha$ values deter-

mined from the gravimetric data. The geometry of the samples (thin rectangular or square foils with known thickness) was explicitly taken into account (e.g., see Fegley *et al.* 1995).

In the case of linear kinetics, all sides of the foils are constantly diminished by $-2k_l't$ as the reaction proceeds with time ($t$) and the remaining volume ($V_t$) becomes smaller. The linear rate constant $k_l'$ (cm hr$^{-1}$) is related to $k_l$ by

$$k_l = (\rho_{Fe} M_S / M_{Fe}) k_l' = 4.51\, k_l', \tag{12}$$

where $\rho_{Fe}$ is the density of Fe metal, and $M_S$ and $M_{Fe}$ are the atomic weights of S and Fe, respectively. The fraction of Fe left ($1 - \alpha$) is related to the remaining volume of Fe by (Brown *et al.* 1980)

$$(1 - \alpha) = \frac{V_t}{V_0} = \frac{(a_0 - 2k_l't)}{a_0} \frac{(b_0 - 2k_l't)}{b_0} \frac{(c_0 - 2k_l't)}{c_0}, \tag{13}$$

where $V_0$ is the initial volume and $a_0$, $b_0$, and $c_0$ are the initial dimensions of the Fe foil. If $a_0 = b_0 = c_0$ then Eq. (13) becomes the well known contracting volume equation (Brown *et al.* 1980)

$$(1 - \alpha)^{1/3} = 1 - 2k_l't/a_0 = 1 - k_l''t \tag{14}$$

However, our samples are not cubes, but are thin rectangular or square foils with $a_0 \sim b_0 \gg c_0$ (see Table III). An approximate solution to Eq. (13) for $k_l'$ is possible because, especially during the initial stages of reaction, $a_0 \sim b_0 \gg k_l't$. Thus, $(a_0 - 2k_l't)/a_0 \sim (b_0 - 2k_l't)/b_0 \sim 1$ and Eq. (13) can be simplified to

$$(1 - \alpha) \sim (c_0 - 2k_l't)/c_0 = 1 - 2(k_l'/c_0)t \tag{15}$$

Equation (15) implies zero-order kinetics (i.e., linear advance of the reaction interface with time) and, as demonstrated by Fig. 12, is a fairly good approximation.

However, especially during the later stages of reaction, the approximations made in deriving Eq. (15) become less accurate. We explicitly considered the three dimensional geometry of the thin foils and solved Eq. (13) for $k_l'$ using the cubic equation (Fegley *et al.* 1995)

$$(k_l')^3 - \frac{L_0}{2t}(k_l')^2 + \frac{A_0}{8t^2} k_l' - \frac{\alpha V_0}{8t^3} = 0, \tag{16}$$

where $L_0 = a_0 + b_0 + c_0$, $A_0 = 2(a_0b_0 + a_0c_0 + b_0c_0)$, and $V_0 = a_0b_0c_0$. The unweighted means of the apparent linear rate constants ($k_l'$) for each gas mixture and temperature are given in Table VI.

**TABLE VI**
**Linear Rate Constants and Iron Grain Lifetimes**

| T (K) | Rate Constant k[a] (cm/hour) | Metal Lifetime[a] (years/cm) |
|---|---|---|
| | **50 ppm $H_2S$** | |
| 558[b] | $(1.50\pm0.49)10^{-6}$ | 76±25 |
| 613[b] | $(2.66\pm0.50)10^{-6}$ | 43±8 |
| 643[c] | $(1.84\pm0.80)10^{-7}$ | 620±270 |
| 673[c] | $(5.64\pm5.33)10^{-7}$ | 202±191 |
| | **100 ppm $H_2S$** | |
| 558 | $(3.88\pm2.50)10^{-7}$ | 294±189 |
| 658 | $(1.59\pm0.14)10^{-6}$ | 72±6 |
| 723 | $(4.62\pm3.45)10^{-6}$ | 25±19 |
| *Activation Energy: 49±5 kJ/mole* | | |
| | **1000 ppm $H_2S$** | |
| 673 | $(3.14\pm0.23)10^{-5}$ | 3.6±0.3 |
| 778 | $(6.85\pm2.48)10^{-5}$ | 1.7±0.6 |
| 848 | $(1.26\pm1.23)10^{-4}$ | 0.91±0.89 |
| 923 | $(1.05\pm0.54)10^{-4}$ | 1.1±0.6 |
| *Activation Energy: 28±7 kJ/mole* | | |
| | **10,000 ppm $H_2S$** | |
| 558 | $(1.87\pm0.51)10^{-5}$ | 6.1±1.7 |
| 673 | $(2.35\pm1.94)10^{-5}$ | 4.9±4.0 |

[a] Errors are $\pm1\sigma$.
[b] Growth along a-axis.
[c] Growth along c-axis.

In the case of parabolic kinetics, the thickness of each side of the foil is decreased by $-\sqrt{2k_p't}$, where $k_p'$ (cm$^2$ hr$^{-1}$) is related to $k_p$ (g$^2$ cm$^{-4}$ hr$^{-1}$) by

$$k_p = (\rho_{Fe} M_S / M_{Fe})^2 k_p' = 20.3\, k_p' \tag{17}$$

The fraction of Fe left ($1 - \alpha$) is related to the remaining volume by the equation

$$(1 - \alpha) = \frac{V_t}{V_0} = \frac{a_0 - \sqrt{2k_p't}}{a_0} \frac{b_0 - \sqrt{2k_p't}}{b_0} \frac{c_0 - \sqrt{2k_p't}}{c_0} \tag{18}$$

which can be simplified to

$$(1 - \alpha) = 1 - \frac{\sqrt{2k_p't}}{c_0} \tag{19}$$

**TABLE VII**
**Parabolic Rate Constants**

| T (K) | Rate Constant k[a] ($cm^2$/hour) |
|---|---|
| **1000 ppm $H_2S$** | |
| 673 | $(9.83\pm9.83)10^{-8}$ |
| 778 | $(1.29\pm0.79)10^{-7}$ |
| 848 | $(5.34\pm3.30)10^{-7}$ |
| 923 | $(4.94\pm0.37)10^{-7}$ |
| *Activation Energy: 38±13 kJ/mole* | |
| **10,000 ppm $H_2S$** | |
| 558 | $(4.58\pm0.43)10^{-8}$ |
| 923 | $(9.31\pm3.61)10^{-6}$ |
| 1173[b] | $(5.77)10^{-5}$ |
| *Activation Energy: 63±1 kJ/mole* | |

[a] Errors are $\pm1\sigma$.
[b] Only one data point.

by assuming that $(a_0 - \sqrt{2k_p't})/a_0 \sim (b_0 - \sqrt{2k_p't})/b_0 \sim 1$. Although this approximation is valid during the initial stages of reaction, it breaks down at large $\alpha$ values when most of the Fe has reacted. We therefore calculated all the parabolic rate constants using an exact solution to Eq. (18). This cubic equation is

$$(k_p'')^3 - (k_p'')^2\left(\frac{t^{2/3}L_0}{\sqrt{2}}\right) + (k_p'')\left(\frac{t^{1/3}A_0}{4}\right) - \left(\frac{\alpha t^{2/3}V_0}{2\sqrt{2}}\right) = 0, \quad (20)$$

where $k_p'' = (k_p')^{1/2}$. The unweighted means of the parabolic rate constants ($k_p'$) for each gas mixture and temperature are listed in Table VII. Figures 13–16 were used to determine which samples display linear or parabolic kinetics.

Some of our experimental conditions are comparable to those of previous studies. Figure 18 compares our linear rate constants (923 K) with data at 943 K from Worrell and Turkdogan (1968). Our experiments were done at much lower sulfur fugacities than those used by Worrell and Turkdogan but extrapolation of their data to our conditions yields good agreement. We also compared our parabolic rate constant for samples formed at 1173 K in 10,000 ppmv $H_2S$ with data from Fryt *et al.* (1979a) and Worrell and Turkdogan (1968). Our rate constant is consistent with extrapolations of their data obtained in more concentrated $H_2S/H_2$ mixtures.

(*d*) *Linear kinetics.* The apparent linear rate constants in Table VI vary with the $H_2S$ content of the gas showing that $H_2S$ is involved in the rate law. Our measurements give the net FeS formation rate,

$$d(\text{FeS})/dt = d(\Delta w/A)/dt = k_l = R_f - R_r \quad (21)$$

(cm $hr^{-1}$ or gs $cm^{-2}$ $hr^{-1}$ depending on whether $k_l'$ or $k_l$ is used), where $R_f$ is the forward rate of reaction (FeS formation), and $R_r$ is the reverse rate of reaction (FeS reduction by $H_2$ in the gas) (e.g., see Haugen and Sterten 1971). Prior work (Worrell 1971; Worrell and Turkdogan 1968) on FeS formation and reduction in $H_2S/H_2$ gas mixtures (1–70% $H_2S$ at 670 to 900°C) shows that FeS formation via Eq. 1 is an opposing first order reaction (Benson 1960). Iron sulfide formation in $COS/CO_2/CO$ gas mixtures is also an opposing first order reaction (Haugen and Sterten 1971; Sterten and Haugen 1973). We rewrite Eq. (21) as

$$d(\text{FeS})/dt = R_f - R_r = k_f P_{H_2S} - k_r P_{H_2}, \quad (22)$$

where $k_f$ is the forward rate constant for FeS formation, $k_r$ is the reverse rate constant for FeS reduction and $P_i$ is the partial pressure of gas *i*. The rate constants have units of cm $hr^{-1}$ $atm^{-1}$ or g $cm^{-2}$ $hr^{-1}$ $atm^{-1}$.

When rate measurements are made far from equilibrium (i.e., $H_2S/H_2$ ratios greater than the equilibrium ratio at the Fe–FeS boundary), Eq. (22) reduces to

$$d(\text{FeS})/dt \sim k_f P_{H_2S} = k_l \quad (23)$$

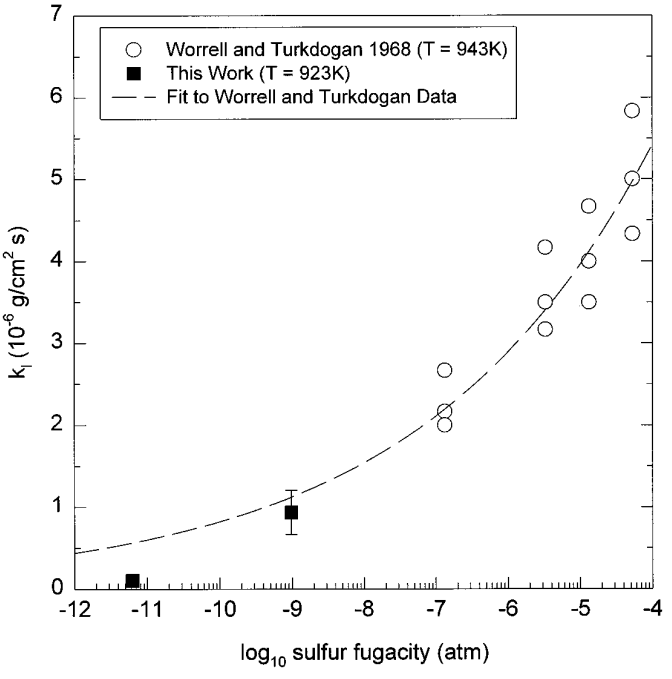


**FIG. 18.** A plot of our linear rate constants ($k_l$) compared to data from Worrell and Torkdogan (1968). The dashed curve is a fit to their data.

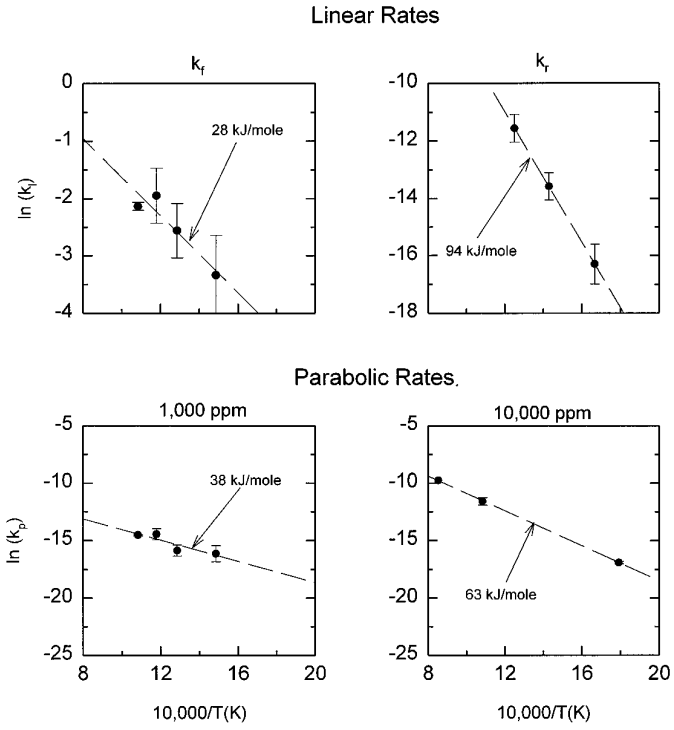


**FIG. 19.** Arrhenius plots for the calculation of the activation energy ($E_a$) for linear ($k_f$ and $k_r$) and parabolic ($k_p$) kinetics. The $E_a$ values for parabolic kinetics are functions of the sulfur fugacity.

and $k_f$ can be calculated. We used the linear rate constants for the ~1000 ppmv $H_2S$ experiments to determine $k_f$ and checked the results using plots of $k_l$ versus $P_{H_2S}$ (e.g., see Haugen and Sterten 1971). The linear rate constants in the ~10,000 ppmv $H_2S$ mixtures do not fall on the same line of $k_l$ versus $P_{H_2S}$ as the ~25 to ~1000 ppmv mixtures and apparently refer to a different reaction mechanism.

The temperature dependence of $k_f$ was calculated from the Arrhenius equation and is

$$k_f = 5.6(\pm 1.3)\exp(-27950(\pm 7280)/RT) \qquad (24)$$

where the activation energy ($E_a$) is ~28 kJ mole$^{-1}$. We calculated $k_r$, the reverse rate constant from $K_l = k_f/k_r$ (Benson 1960) where $K_l$ is the equilibrium constant for reaction (1). The temperature dependence of $k_r$ is

$$k_r = 10.3(\pm 1.0)\exp(-92610(\pm 350)/RT) \qquad (25)$$

and the activation energy is ~93 kJ mole$^{-1}$. The plots for $k_f$ and $k_r$ are shown in Fig. 19.

As noted above, plots of the apparent linear rate constants (Table VI) versus $P_{H_2S}$ yield straight lines for low concentration (≤1000 ppmv) $H_2S$ gas mixtures, but the apparent linear rate constants for the ~10,000 ppmv $H_2S$ mixtures do not fall on the same lines. This behavior is qualitatively similar to a Langmuir adsorption isotherm (Benson 1960)

$$\theta_{H_2S} = KP_{H_2S}/(1 + KP_{H_2S}), \qquad (26)$$

where $\theta_{H_2S}$ is the fractional coverage of the Fe (or FeS) surface by adsorbed $H_2S$ and $K$ is the equilibrium constant for adsorption. At low $H_2S$ partial pressures, $KP_{H_2S} \ll 1$ and the adsorption isotherm reduces to $\theta_{H_2S} \sim KP_{H_2S}$. At high $H_2S$ partial pressures, $KP_{H_2S} \gg 1$ and the adsorption isotherm becomes $\theta_{H_2S} \sim 1$. There is also a similarity to $H_2S$ adsorption isotherms on Cu and Ag metal surfaces (Worrell 1971). We suggest that $H_2S$ adsorption on the Fe (or FeS) surface is the rate limiting step in the low concentration (~25 to ~1000 ppmv) $H_2S$ gas mixtures, but that another process is rate limiting at higher $H_2S$ concentrations (e.g., Worell and Turkdogan 1968).

(*e*) *Parabolic kinetics.* Metallurgical studies of FeS formation in sulfur vapor and $H_2S/H_2$ gas mixtures (Table IV) and measurements of the Fe and S diffusion coefficients in iron sulfide (Condit *et al.* 1974) show that $Fe^{2+}$ diffusion in the sulfide layer is the rate limiting step for parabolic iron sulfide formation. The $Fe^{2+}$ diffusion coefficient ($D$) is a function of the temperature and sulfide stoichiometry (Condit *et al.* 1974)

$$D = D_0\delta \exp\{-[81(\pm 4) + 84(\pm 20)\delta]/RT\} \qquad (27)$$

where $D_0$ is 1.7(±0.1) × 10$^{-2}$ and 3.0(±0.2) × 10$^{-2}$ cm$^2$ sec$^{-1}$ for diffusion along the *a* and *c* crystallographic axes, respectively. This relationship arises because the Fe vacancy concentration ($\delta$) is a function of temperature and sulfur fugacity (e.g., Libowitz 1972). Thus the activation energy for parabolic FeS formation also varies with temperature and sulfur fugacity.

The two $E_a$ values from Arrhenius plots (Fig. 19) of the parabolic rate constants are 38±13 kJ mole$^{-1}$ and 63±1 kJ mole$^{-1}$ in the nominal 1,000 and 10,000 ppmv $H_2S$ gas mixtures respectively. The small uncertainty on the $E_a$ value for the 10,000 ppmv mixtures is due to having only a single rate determination at 1173 K. Fryt *et al.* (1979a) summarize $E_a$ values for parabolic Fe sulfurization kinetics and tabulate values of ~(8–12) kJ mole$^{-1}$ for sulfides close to FeS and values ~(70–80) kJ mole$^{-1}$ for pyrrhotites around $Fe_{0.90}S$. Our calculated activation energies display a qualitatively similar trend. The samples formed in ~1,000 ppmv $H_2S$ mixtures have $E_a \sim 38$ kJ mole$^{-1}$ and sulfide compositions of $Fe_{0.99}S$. The samples formed in ~10,000 ppmv $H_2S$ mixtures have $E_a \sim 63$ kJ mole$^{-1}$ and sulfide compositions of $Fe_{0.94}S$ to $Fe_{0.99}S$.

Because $Fe^{2+}$ diffusion is rate limiting for the parabolic growth of FeS layers, we used our parabolic rate constants to calculate the $Fe^{2+}$ diffusion coefficient. The parabolic

**TABLE VIII**
**Iron Diffusion Coefficients ($cm^2$ $sec^{-1}$) in $Fe_{1-\delta}S$**

| T (K) | 1-δ in $Fe_{1-\delta}S$[b] | $k'_p$ ($cm^2$ $hour^{-1}$) | $D_{Fe}$ (This work) | $D_{Fe}$ (Condit et al)[a] |
|---|---|---|---|---|
| 673 | 0.988 | $(9.83\pm9.83)10^{-8}$ | $(1.89\pm1.89)10^{-11}$ | $(8.80)10^{-11}$ |
| 778 | 0.990 | $(1.29\pm0.79)10^{-7}$ | $(3.29\pm2.01)10^{-11}$ | $(5.44)10^{-10}$ |
| 848 | 0.989 | $(5.34\pm3.30)10^{-7}$ | $(1.61\pm0.99)10^{-10}$ | $(8.73)10^{-10}$ |
| 923 | 0.990[c] | $(4.94\pm0.37)10^{-7}$ | $(1.76\pm0.13)10^{-10}$ | $(3.97)10^{-9}$ |
| 923 | 0.985[c] | $(9.31\pm3.61)10^{-6}$ | $(3.34\pm1.30)10^{-9}$ | $(5.64)10^{-9}$ |
| 1173 | 0.988 | $(5.77)10^{-5}$ | $(3.30)10^{-8}$ | $(4.55)10^{-8}$ |

[a] Calculated from Eq. (27). The uncertainties are ~ ±50% of the $D_{Fe}$ value tabulated.
[b] The mean Fe/S ratios from Table 3.
[c] $1 - \delta$ is 0.990 for ~1000 ppm $H_2S$ and 0.988 for ~10,000 ppm $H_2S$.

rate constant $k'_p$ is related to the iron ($D_{Fe}$) and sulfur ($D_S$) diffusion coefficients by (Schmalzried 1974)

$$k'_p = \frac{1}{RT}\int_{\mu_{Fe(gas)}}^{\mu^0_{Fe}} (D_{Fe} + D_S)\, d\mu_{Fe} \qquad (28)$$

The integration in Eq. (28) extends from the metal–sulfide interface where the chemical potential of Fe metal is $\mu^0_{Fe}$ to the sulfide–gas interface where the chemical potential of the metal is $\mu_{Fe}$(gas). The experimental data of Condit *et al.* (1974) show that sulfur diffusion in iron sulfide is much slower than Fe diffusion. Thus, the $D_S$ term in Eq. (28) is neglected in the rest of this treatment. Following Schmalzried (1974) the average $Fe^{2+}$ diffusion coefficient is defined as

$$\overline{D}_{Fe} = \frac{1}{\mu^0_{Fe} - \mu_{Fe(gas)}}\int_{\mu_{Fe(gas)}}^{\mu^0_{Fe}} D_{Fe}\, d\mu_{Fe}, \qquad (29)$$

where the average is taken with respect to chemical potential across the layer. Combining Eqs. (28–29), and rewriting in terms of the Gibbs free energy of formation of FeS ($\Delta G_{FeS}$) yields

$$k'_p = \overline{D}_{Fe}\frac{|\Delta G_{FeS}|}{RT} \qquad (30)$$

for the average $Fe^{2+}$ diffusion coefficient across the sulfide layer.

We evaluated Eq. (30) for sulfide layers formed in the parabolic regime in the ~1,000 ppmv and ~10,000 ppmv $H_2S$ mixtures. The mean Fe/S ratios of the sulfide layers were taken from Table V and the thermodynamic data of Grønvold and Stølen (1992) were used to calculate the Gibbs free energy of formation of $Fe_{1-\delta}S$ ($\Delta G_{FeS}$) as a function of the Fe/S ratio. Table VIII lists our results and also shows the Fe diffusion coefficients calculated from Eq. (27). There is fair agreement with the literature diffusion coefficient (Condit *et al.* 1974).

## IRON SULFIDE FORMATION KINETICS IN THE SOLAR NEBULA

We used our experimentally determined rate constants to calculate the rate of iron sulfide formation in the solar nebula. We assumed that the iron sulfide formation rate from solar composition $Fe_{95}Ni_5$ alloy is not significantly different than from pure Fe metal. Our preliminary study of sulfidation kinetics for meteoritic $Fe_{94}Ni_6$ metal (Lauretta *et al.* 1995a) shows that the sulfidation rate for the alloy is about 90% of that for pure Fe metal under the same conditions (~923 K and ~10,000 ppmv $H_2S$) and indicates that this assumption is valid.

We first calculated the thickness of sulfide rims that can form around metal grains to determine the grain sizes for which diffusion eventually becomes rate limiting. If we assume that all grains are spherical the volume of sulfide is directly related to the extent of reaction by:

$$V_{sulfide} = M_{v,FeS} \times P \times \tfrac{4}{3}\pi r^3 / M_{v,Fe}, \qquad (31)$$

where $M_{v,FeS}$ is the molar volume of iron sulfide (18.20 $cm^3$), $P$ is the percent of the grain reacted, $r$ is the initial radius of the metal grain, and $M_{v,Fe}$ is the molar volume of iron metal (7.09 $cm^3$). The volume and thickness of the sulfide are given by

$$V_{sulfide} = \tfrac{4}{3}\pi(r^3_{grain} - r^3_{metal}) \qquad (32)$$

$$t_{layer} = r_{grain} - r_{metal}. \qquad (33)$$

Figure 20 shows the results of the calculations and the range of experimentally determined critical thickness values from Fig. 17. Iron grains smaller than 10 $\mu$m in radius will never develop sulfide layers thicker than the critical

thickness at which diffusion becomes rate limiting. Thus, iron sulfide formation on these small grains will always follow linear kinetics. Initially, iron sulfide formation on 10 $\mu$m radius iron grains follows linear kinetics but later makes a transition to parabolic kinetics after ~90% of the grain has reacted. Likewise, the sulfidation of 100 $\mu$m radius iron grains switches to parabolic kinetics after ~10% of the grain has reacted, and 1000 $\mu$m radius grains follow parabolic kinetics after only ~3% reaction. Iron sulfide formation on larger iron grains essentially follows parabolic kinetics at all times.

Adopting the commonly held assumption that chondritic meteorites contain at least some pristine nebular material, Kerridge (1993) used petrographic information on the sizes of different components in chondrites to qualitatively estimate grain sizes in the solar nebula. The matrix of type 3 chondrites has grain sizes of 0.05–10 $\mu$m, while metal in type 3 and 4 chondrites has grain sizes of <40 $\mu$m to >400 $\mu$m (Kerridge 1993). We therefore considered the sulfidation of 10 $\mu$m and 1000 $\mu$m radius iron grains as endmember cases to illustrate a range of timescales.

The linear rate equation for sulfidation of Fe grains (<10 $\mu$m radius) is

$$d(\mathrm{FeS})/dt = k_f P_{H_2S} - k_r P_{H_2} \qquad (22)$$

cm hr$^{-1}$. Using our experimentally determined values for the forward and reverse rate constants (Eq. 24 and 25) we calculate that 10 $\mu$m radius grains are completely converted to iron sulfide in ~200 years at 700 K and $10^{-3}$ atm. This temperature is ~10° below the (pressure independent) troilite condensation point. The pressure of $10^{-3}$ atm is commonly used in nebular condensation calculations by many authors. Equation (22) shows that the sulfidation rate is linearly dependent on the total pressure (for a solar composition gas). Thus lower assumed total pressures will lead to correspondingly decreased sulfidation rates and increased times required for complete sulfidation. Currently estimated nebular lifetimes are 0.1–10 million years (Podosek and Cassen 1994). Thus, unless total pressures in the inner solar nebula were always below $10^{-6}$ atm in the 400–720 K region, sulfidation of 10 $\mu$m radius (and smaller) iron grains would have gone to completion within the lifetime of the solar nebula.

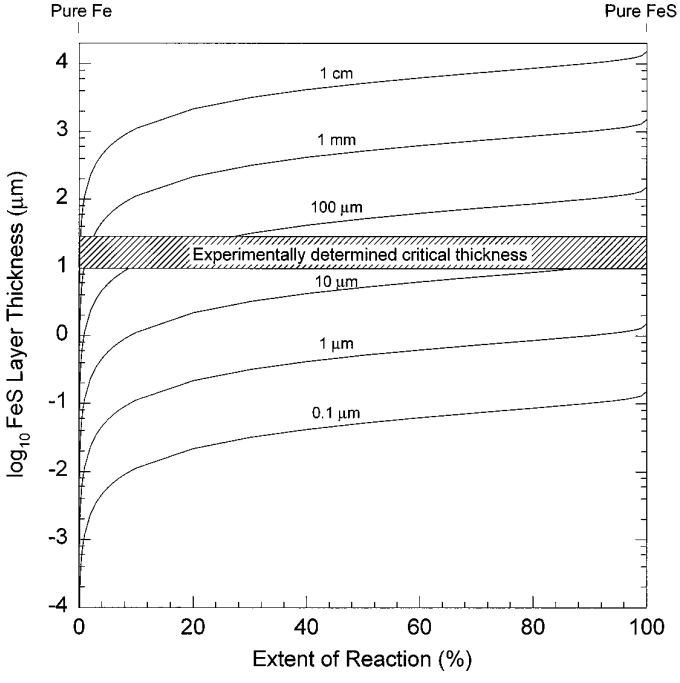


**FIG. 20.** A plot showing the calculated thickness of FeS layers formed on spherical Fe grains. Comparison with the experimentally determined critical layer thickness indicates that diffusion controlled kinetics is unimportant for grains less than 10 $\mu$m in radius.

The parabolic rate equation for sulfidation of Fe grains (>10 $\mu$m radius) in the solar nebula is given by

$$[(dx)^2/dt] = k_p' \sim \overline{D}_{Fe} \qquad (34)$$

cm$^2$ hr$^{-1}$. Our previous discussion showed that parabolic sulfidation rates vary with both the temperature and sulfide composition, but they do not vary with the total pressure. Assuming a nearly stoichiometric sulfide with Fe/S = 0.999, taking $T$ = 700 K, and $D_{Fe}$ from Eq. (27), we calculate that 1000 $\mu$m radius iron grains will be completely converted to iron sulfide in ~500 years. Because of the strong dependence of the iron diffusion coefficient on the sulfide composition, Fe deficient pyrrhotites, if stable, would form more rapidly.

The calculations above use the laboratory rate constants to model iron sulfide formation kinetics in the solar nebula. However, the rate limiting step for linear kinetics may change in going from ~1 atmosphere pressure to pressures of $10^{-3}$ to $10^{-6}$ atmospheres in the inner solar nebula (e.g., see Fegley and Prinn 1989). In this case $H_2S$ adsorption on Fe metal may no longer be rate limiting and instead the supply of gas molecules to the metal may be rate limiting. If this is the case then a model of the gas–grain collision frequency is needed to determine the lifetime.

As described earlier, Fegley (1988) developed a simple collision theory (SCT) model for the kinetics of chemical reactions between gases and grains in the solar nebula. We apply this model using our experimentally determined value of ~28 kJ mole$^{-1}$ for the activation energy of iron sulfide formation. The collision rate of the reactant gas with the grain surfaces is given by

$$\sigma_i = 2.635x10^{25}\left[\frac{P_i}{(M_i T)^{1/2}}\right] \qquad (35)$$

(molecules cm$^{-2}$ s$^{-1}$) where $P_i$ is the partial pressure of

reactant gas $i$ and $M_i$ is the molecular weight of gas $i$. The total number of collisions with all grains in each cm$^3$ is given by

$$v_i = \sigma_i A \tag{36}$$

(molecules cm$^{-3}$ s$^{-1}$) where $A$ is the total surface area of all reactant grains per each cm$^3$ of the nebula. Spherical grains with radii of either 0.1 $\mu$m or 1000 $\mu$m are assumed to be uniformly distributed at solar abundance within the gas. Only a fraction of the gas particles that collide with the grains have the necessary activation energy to react with the metal. This is given by

$$f_i = \exp\left(\frac{-E_a}{RT}\right). \tag{37}$$

As the reaction progresses the gas is depleted in the reactant species and the collisions become less frequent. To take this into account we performed successive iterations using the above formulas at each stage. For each time step the amount of $H_2S$ left in the gas is calculated as

$$N_{H_2S,t} = N_{H_2S,t-1} - c \exp\left(\frac{-E_a}{RT}\right) \frac{P_{H_2S,t-1}}{T^{1/2}} \Delta t, \tag{38}$$

where $N$ represents the total number of molecules of $H_2S$ left in the gas, $c$ is a constant from Eq. (35), and $\Delta t$ is the time step between each iteration. The total number of molecules per unit volume at any time is equal to the amount present minus the number that react to form sulfide. The results of these calculations are shown in Fig. 21. This figure shows that all (0.1 $\mu$m grains) or a large percentage (1000 $\mu$m grains) of the $H_2S$ in solar composition gas can be quantitatively condensed into iron sulfide within the estimated nebular lifetime of 0.1–10 million years.

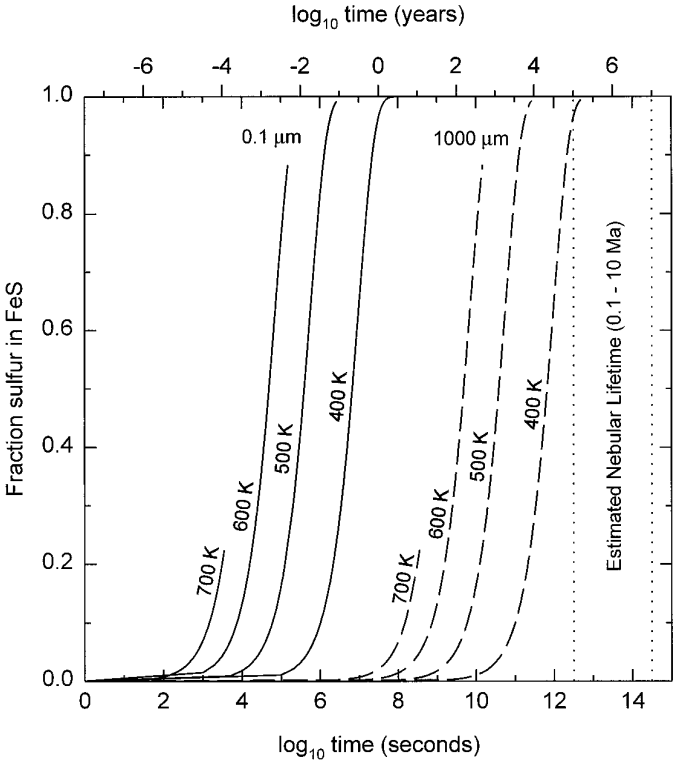


**FIG. 21.** A graph showing $H_2S$ lifetimes in the solar nebula at various temperatures. Lifetimes are based on gas molecule collision frequency with monodispersed Fe grains having radii of 0.1 $\mu$m (solid lines) and 1000 $\mu$m (dashed lines). In both cases all the $H_2S$ will react to form FeS within the estimated lifetime of the solar nebula (dotted lines).

## METEORITIC PYRRHOTITE

Although troilite is the most common sulfide in meteorites, pyrrhotite ~$(Fe, Ni)_{0.9}S$ with Fe/Ni ~ 50 is a common, if not the most common, sulfide in CI carbonaceous chondrites (e.g., Kerridge 1970, 1976; Kerridge *et al.* 1979). Iron sulfides with compositions ranging from ~$Fe_{1.1}S$ to ~$Fe_{0.8}S$ are also observed in chondritic anhydrous and hydrated interplanetary dust particles (e.g., Zolensky and Thomas 1995). Here we briefly discuss the origin of pyrrhotite in chondrites and interplanetary dust particles (IDPs).

Our experiments produced iron sulfides with compositions varying from $Fe_{0.90}S$ to FeS with temperature and $H_2S/H_2$ ratio in agreement with thermodynamic calculations (see Table V). This implies that iron sulfides formed in the solar nebula will also have compositions in equilibrium with the gas. We calculated the range of sulfide compositions in equilibrium with solar composition gas ($H_2S/H_2$ ~33 ppmv) as a function of temperature from ~713 K, the troilite formation temperature, to 400 K, the magnetite formation temperature to be $Fe_{0.97}S$ to FeS.

Qualitatively, these calculations support the suggestion that the reaction

$$9FeS + H_2S = Fe_9S_{10} + H_2 \tag{39}$$

could lead to pyrrhotite formation in the solar nebula (Kerridge 1976; Zolensky and Thomas 1995). However, subsequently Kerridge *et al.* (1979) showed that the sulfides in the Orgueil CI chondrite are probably secondary alteration products. Also, the Fe/S ratios of pyrrhotites in IDP's are lower than those predicted by our calculations.

Fegley and Palme (1985) discussed the chemistry of sulfur-rich regions of the solar nebula, and their results illustrate that reheating of dust-rich regions in the solar nebula will lead to sulfur fugacities above those fixed by the solar $H_2S/H_2$ ratio. For example, increasing the dust/gas ratio to 100 times the solar value leads to production of pyrrhotites

ranging from $Fe_{0.98}S$ (at 700 K) to $Fe_{0.94}S$ (at 400 K). Lower Fe/S ratios maybe due to higher dust/gas ratios or simply to failure of gas and grains to completely equilibrate. For example, our experiments at 558 K in ~50 ppmv $H_2S$ led to Fe/S ~0.96 versus the predicted equilibrium value of ~0.99.

## METEORITIC TROILITE

Finally, we apply our results to the identification of pristine nebular sulfide condensates in chondrites. This work and our study of the sulfidation of meteoritic FeNi metal (Lauretta *et al.* 1995b), provide necessary criteria for classifying meteoritic metal–sulfide assemblages in chondrites as pristine nebular condensates. The large variation in the growth structure of the sulfide layers indicates that the sulfide morphology alone cannot be used to identify a natural sample as a pristine nebular condensate. Instead of basing contentions for such condensates solely on textural arguments, it is also necessary to take chemical considerations into account. The sulfidation of iron and iron–nickel alloys creates several distinctive chemical fractionation patterns that can assist in the identification of nebular sulfide material. First, the stoichiometry of the sulfide layer is not constant. Instead, we find that the total metal to sulfur ratio decreases with distance from the metal. In addition, the fractionation of nickel is very distinctive. Typically, a thin band of metal near the sulfide is enriched in nickel. Also, significant amounts of nickel are present in the sulfide layer and the nickel content of the sulfide increases away from the metal. Any identification of pristine nebular sulfide material should consider these distinguishing fractionation patterns.

## ACKNOWLEDGMENTS

This work was supported by NASA Grant NAGW-3070. We thank K. Lodders and R. Poli for advice and technical assistance.

## REFERENCES

Anders, E., and N. Grevesse 1989. Abundances of the elements: Meteoritic and solar. *Geochim. Cosmochim. Acta* **53,** 197–214.

Armstrong, J. T. 1988. Quantitative analysis of silicate and oxide minerals: Comparison of Monte-Carlo, ZAF and Phi-Rho-Z procedures. *Microbeam Anal.* **23,** 239–246.

Arnold, R. G. 1962. Equilibrium relations between pyrrhotite and pyrite from 325 to 743°C. *Econ. Geol.* **57,** 72–90.

Barker, W. W., and T. C. Parks 1986. The thermodynamic properties of pyrrhotite and pyrite: A re-evaluation. *Geochim. Cosmochim. Acta* **50,** 2185–2194.

Benson, S. W. 1960. *The Foundations of Chemical Kinetics.* McGraw–Hill, New York.

Brown, H. S. 1949. A table of relative abundances of nuclear species. *Rev. Mod. Phys.* **21,** 625–634.

Brown, M. E., D. Dollimore, and A. K. Galwey 1980. Theory of solid state reaction kinetics. In *Comprehensive Chemical Kinetics* (C. H. Bamford and C. F. H. Tipper, Eds.), Vol. 22, pp. 41–113. Elsevier, Amsterdam.

Burgmann, W., Jr., G. Urbain, and M. G. Frohberg 1968. Contribution à l'étude du système fer–soufre limité du domaine du mono-sulfure de fer (pyrrhotine). *Mem. Sci. Rev. Métall.* **65,** 567–578.

Cameron, A. G. W. 1968. A new table of abundances of the elements of the solar system. In *Origin and Distribution of the Elements* (L. H. Ahrens, Ed.), pp. 125–143, Pergamon, Oxford.

Cemic, L., and O. J. Kleppa 1988. High temperature calorimetry of sulfide systems. III. Standard enthalpies of formation of phases in the systems Fe–Cu–S and Co–S. *Phys. Chem. Miner.* **16,** 172–179.

Chase, M. W., Jr., C. A. Davies, J. R. Downey, Jr., D. J. Frurip, R. A. McDonald, and A. N. Syverud 1985. *JANAF Thermochemical Tables,* 3rd ed. *J. Phys. Chem. Ref. Data* **14,** suppl. no. 1.

Condit, R. H., R. R. Hobbins, and C. E. Birchenall 1974. Self-diffusion of iron and sulfur in ferrous sulfide. *Oxid. Met.* **8,** 409–455.

Darken, L. S., and R. W. Gurry 1945. The system iron–oxygen. I. The wüstite field and related equilibria. *J. Am. Chem. Soc.* **67,** 1398–1412.

Dreibus, G., H. Palme, B. Spettel, J. Zipfel, and H. Wänke 1995. Sulfur and selenium in chondritic meteorites. *Meteoritics* **30,** 439–445.

Evans, H. T., Jr., D. E. Appleman, and D. S. Handwerker 1973. Report PB216188, NTIS.

Fegley, B., Jr. 1988. Cosmochemical trends of volatile elements in the solar system. In *Workshop on the Origins of Solar Systems* (J. A. Nuth and P. Sylvester, Ed.), LPI Technical Report No. 88-04, pp. 51–60.

Fegley, B., Jr. 1993. Chemistry of the solar nebula. In *The Chemistry of Life's Origins* (M. Greenberg, C. X. Mendoza-Gomez, and V. Pirronello, Eds.), pp. 75–147. Dordrecht.

Fegley, B., Jr., K. Lodders, A. H. Treiman, and G. Klingelhöfer 1995. The rate of pyrite decomposition on the surface of Venus. *Icarus* **115,** 159–180.

Fegley, B., Jr., and R. G. Prinn 1989. Solar nebula chemistry: Implications for volatiles in the Solar System. In *The Formation and Evolution of Planetary Systems* (H. Weaver and L. Danly, Eds.), pp. 171–211. Cambridge Univ. Press, Cambridge, UK.

Fegley, B., Jr., and H. Palme 1985. Evidence for oxidizing conditions in the solar nebula from Mo and W depletions in refractory inclusions in carbonaceous chondrites. *Earth Planet. Sci. Lett.* **72,** 311–326.

Fegley, B., Jr., D. S. Lauretta, and D. T. Kremser 1995. The origin of troilite and pyrrhotite in chondrites. I. Iron sulfide formation kinetics in $H_2S$-$H_2$ gas mixtures [abstract] In abstract volume, 20th Symposium on Antarctic Meteorites, Tokyo, Japan, pp. 59–62.

Fleet, M. E. 1968. On the lattice parameters and superstructures of pyrrhotites. *Am. Mineral.* **53,** 1846–1855.

Frondel, J. W. 1975. *Lunar Mineralogy.* Wiley–Interscience, New York.

Fryt, E. M., V. S. Bhide, W. W. Smeltzer, and J. S. Kirkaldy 1979a. Growth of the iron sulfide ($Fe_{1-\delta}S$) scale on iron at temperatures 600°–1000°C. *J. Electrochem. Soc.* **126,** 683–688.

Fryt, E. M., W. W. Smeltzer, and J. S. Kirkaldy 1979b. Chemical diffusion and point defect properties of iron sulfide ($Fe_{1-\delta}S$) at temperatures 600°–1000°C. *J. Electrochem. Soc.* **126,** 673–683.

Grønvold, F., S. Stølen, A. K. Labban, and E. F. Westrum, Jr. 1991. Thermodynamics of iron sulfides. I. Heat capacity and thermodynamic properties of $Fe_9S_{10}$ at temperatures from 5 K to 740 K. *J. Chem. Thermodyn* **23,** 261–272.

Grønvold, F., and S. Stølen 1992. Thermodynamics of iron sulfides. II. Heat capacity and thermodynamic properties of FeS and of $Fe_{0.875}S$ at temperatures from 298.15 K to 1000 K, of $Fe_{0.98}S$ from 298.15 K to

800 K, and of $Fe_{0.89}S$ from 298.15 K to about 650 K. Thermodynamics of formation. *J. Chem. Thermodyn.* **24,** 913–936.

Grossman, L. 1972. Condensation in the primitive solar nebula. *Geochim. Cosmochim. Acta* **36,** 597–619.

Hägg, G., and I. Sucksdorff 1933. Die Kristallstruktur von Troilit und Magnetkies. *Z. Phys. Chem. Teil. B* **22,** 444–452.

Hansen, M., and K. Anderko 1958. *Constitution of Binary Alloys,* 2nd ed. McGraw–Hill, New York.

Haraldsen, H. 1941. Über die Hochtemperaturumwandlungen der Eisen(II)–Sulfidmischkristalle. *Z. Anorg. Allg. Chem.* **246,** 195–226.

Hauffe, K., and A. Rahmel 1952. Uber den Mechanismus der Schwefelung von Eisen, Nickel und Nickellegierungen bei höheren Temperaturen. *Z. Phys. Chem.* **199,** 152–169.

Haugen, S., and A. Sterten 1971. High-temperature linear kinetics of FeS formation and reduction in $COS–CO–CO_2$ gas mixtures. *Oxid. Met.* **3,** 545–555.

Haycock, E. W. 1959. High-temperature sulfiding of iron alloys in hydrogen sulfide–hydrogen mixtures. *J. Electrochem. Soc.* **106,** 764–771.

Horwood, J. L., M. G. Townsend, and A. H. Webster 1976. Magnetic susceptibility of single crystal $Fe_{1-x}S$. *J. Solid State Chem.* **17,** 35–42.

Jamin-Changeart, F., and S. Talbot-Besnard 1965. Rôle de la pureté dans la sulfuration du fer par des mélanges hydrogène sulfuré-argon et quelques précisions sur le mécanisme de formation d'une couche interne de sulfure. *Mem. Sci. Rev. Métall.* **62,** 305–312.

Kelley, K. K. 1949. *Contributions to the Data on Theoretical Metallurgy.* U.S. Bur. Mines Bull. 476, US Govt. Printing Office, Washington. D.C.

Kerridge, J. F. 1970. Meteoritic pyrrhotite. *Meteoritics* **5,** 149–152.

Kerridge, J. F. 1976. Formation of iron sulphide in solar nebula. *Nature* **259,** 189–190.

Kerridge, J. F. 1993. What can meteorites tell us about nebular conditions and processes during planetesimal accretion? *Icarus* **106,** 135–150.

Kerridge, J. F., and M. S. Matthews 1988. *Meteorites and the Early Solar System.* Univ. of Arizona Press, Tucson.

Kerridge, J. F., J. D. MacDougall, and K. Marti 1979. Clues to the origin of sulfide minerals in CI chondrites. *Earth Planet. Sci. Lett.* **43,** 359–367.

Kingery, W. D., H. K. Bowen, and D. R. Uhlmann 1976. *Introduction to Ceramics,* 2nd ed. Wiley–Interscience, New York.

Larimer, J. W. 1967. Chemical fractionations in meteorites. I. Condensation of the elements. *Geochim. Cosmochim. Acta* **31,** 1215–1238.

Larimer, J. W., and E. Anders 1967. Chemical fractionations in meteorites. II. Abundance patterns and their interpretation. *Geochim. Cosmochim. Acta* **31,** 1239–1270.

Lauretta, D. S., and B. Fegley, Jr. 1994a. An experimental study of iron sulfide formation kinetics in $H_2–H_2S$ gas mixtures and applications to iron sulfide condensation in the solar nebula. *Lunar Planet. Sci.* **25,** 773–774.

Lauretta, D. S., and B. Fegley, Jr. 1994b. Troilite formation kinetics and growth mechanism in the solar nebula. *Meteoritics* **29,** 490.

Lauretta, D. S., and B. Fegley, Jr. 1994c. Kinetics and grain growth mechanism for troilite formation on iron metal in $H_2–H_2S$ gas mixtures [abstract]. Abstract volume of the 19th Symposium on Antarctic Meteorites, Tokyo, Japan, pp. 62–65.

Lauretta, D. S., D. T. Kremser, and B. Fegley, Jr. 1995a. Nickel fractionation during troilite formation in the solar nebula. *Lunar Planet. Sci.* **26,** 831–832.

Lauretta, D. S., D. T. Kremser, and B. Fegley, Jr. 1995b. The origin of troilite and pyrrhotite in chondrites. II. Comparative studies of metal–sulfide assemblages [abstract]. Abstract volume of the 20th Symposium on Antarctic Meteorites, Tokyo, Japan, pp. 134–137.

Lewis, J. S. 1972. Metal–silicate fractionation in the solar system. *Earth Planet. Sci. Lett.* **15,** 286–290.

Libowitz, G. G. 1972. Energetics of defect formation and interaction in non-stoichiometric pyrrhotite. In *Reactions of Solids* (J. S. Anderson, M. W. Roberts, and F. S. Stone, Eds.), pp.107–115. Chapman & Hall, London.

Lord, H. C. 1965. Molecular equilibria and condensation in a solar nebula and cool stellar atmospheres. *Icarus* **4,** 279–288.

Meussner, R. A., and C. E. Birchenall 1957. The growth of ferrous sulfide on iron. *Corrosion* **13,** 677t–689t.

Nagamori, M., and M. Kameda 1968. Thermodynamics of pyrrhotite ($Fe_{1-\delta}S$) at the temperature range of 800° ~ 1100°C. *Trans. Jpn. Inst. Met.* **9,** 187–194.

Narita, T., and K. Nishida 1973a. The effect of sulfur pressure on the iron sulfide scale growth at elevated temperature. *Trans. Jpn. Inst. Met.* **14,** 439–446.

Narita, T., and K. Nishida 1973b. On the sulfur distribution in FeS scale formed on pure iron at 700°C. *Trans. Jpn. Inst. Met.* **14,** 447–456.

Niwa, K., and T. Wada 1961. Thermodynamic studies of pyrrhotite. *Metall. Soc. Conf.* **8,** 945–961.

Orchard, J. P., and D. J. Young 1989. Sulfidation behavior of an iron–nickel alloy. *J. Electrochem. Soc.* **136,** 545–550.

Podosek, F. A., and P. Cassen 1994. Theoretical, observational, and isotopic estimates of the lifetime of the solar nebula. *Meteoritics* **29,** 6–25.

Prinn, R. G., and B. Fegley, Jr. 1989. Solar nebula chemistry: Origin of planetary, satellite and cometary volatiles. In *Origin and Evolution of Planetary and Satellite Atmospheres* (S. K. Atreya, J. B. Pollack, and M. S. Matthews, Eds.), pp. 78–136. Univ. of Arizona Press, Tucson.

Rau, H. 1976. Energetics of defect formation and interaction in pyrrhotite $Fe_{1-x}S$ and its homogeneity range. *J. Phys. Chem. Solids* **37,** 425–429.

Richardson, F. D., and J. H. E. Jeffes 1952. The thermodynamics of substances of interest in iron and steel making. III. Sulphides. *J. Iron Steel Inst.* **171,** 165–175.

Robie, R. A., and D. R. Waldbaum 1968. *Thermodynamic Properties of Minerals and Related Substances at 298.15°K (25.0°C) and One Atmosphere (1.013 Bars) Pressure and at Higher Temperatures.* U.S. Geol. Surv. Bull. No. 1259, U.S. Govt. Printing Office, Washington, D.C.

Rosenqvist, T. 1954. A thermodynamic study of the iron, cobalt and nickel sulfides. *J. Iron Steel Inst.* **174,** 37–57.

Rossini, R. A., D. D. Wagman, W. H. Evans, S. Levine, and I. Jaffe 1952. *Selected Values of Chemical Thermodynamic Properties.* NBS Circular 500, U.S. Govt. Printing Office, Washington, D.C.

Schmalzried, H. 1974. *Solid State Reactions* (A. D. Pelton, Transl.). Academic Press, New York.

Sears, D. W. 1978. Condensation and the composition of iron meteorites. *Earth Planet. Sci. Lett.* **41,** 128–138.

Sterten, Å., and S. Haugen 1973. The parabolic rate constant for $Fe_{1-x}S$ formation as a function of sulfur activity. *Oxid. Met.* **7,** 45–54.

Toulmin, P., III, and Barton, P. B. 1964. A thermodynamic study of pyrite and pyrrhotite. *Geochim. Cosmochim. Acta* **28,** 641–671.

Turkdogan, E. T. 1968. Iron–sulfur system. I. Growth rate of ferrous sulfide on iron and diffusivities of iron in ferrous sulfide. *Trans. AIME* **242,** 1665–1672.

Turkdogan, E. T., W. M. McKewan, and L. Zwell 1965. Rate of oxidation of iron to wüstite in water–hydrogen gas mixtures. *J. Phys. Chem.* **69,** 327–334.

Urey, H. C. 1952. *The Planets.* Yale Univ. Press, New Haven, CT.

Wagner, C. 1951. Diffusion and high temperature oxidation of metals. In *Atom Movements,* pp. 153–173. Am. Soc. Met., Cleveland.

WAI, C. M., AND J. T. WASSON 1977. Nebular condensation of moderately volatile elements and their abundances in ordinary chondrites. *Earth Planet. Sci. Lett.* **36,** 1–13.

WILSON, E. B., JR. 1952. *An Introduction to Scientific Research.* McGraw–Hill, New York.

WOOD, J. A., AND A. HASHIMOTO 1993. Mineral equilibrium in fractionated nebular systems. *Geochim. Cosmochim. Acta* **57,** 2377–2388.

WORRELL, W. L. 1971. Dissociation of gaseous molecules on solids at high temperature. In *Advances in High Temperature Chemistry* (L. Eyring, Ed.), Vol. 4, pp. 71–105. Academic Press, New York.

WORRELL, W. L., AND E. T. TURKDOGAN 1968. Iron sulfur system. II. Rate of reaction of hydrogen sulfide with ferrous sulfide. *Trans. AIME* **242,** 1673–1678.

YOUNG, D. J. 1980. The sulfidation of iron and its alloys. *Rev. High Temp. Mater.* **4,** 299–346.

YUND, R. A., AND H. T. HALL 1969. Hexagonal and monoclinic pyrrhotites. *Econ. Geol.* **64,** 420–423.

ZOLENSKY, M. E., AND K. L. THOMAS 1995. Iron- and iron–nickel sulfides in chondritic interplanetary dust particles. *Lunar Planet. Sci.* **26,** 1567–1568.